catalysts

MDPI

Review

Solution Plasma for Surface Design of Advanced Photocatalysts

Rui Wang, Changhua Wang *, Yanmei Xing and Xintong Zhang *

Key Laboratory of UV-Emitting Materials and Technology of Chinese Ministry of Education, Northeast Normal University, 5268 Renmin Street, Changchun 130024, China; wangr132@nenu.edu.cn (R.W.); xingym650@nenu.edu.cn (Y.X.)

* Correspondence: wangch100@nenu.edu.cn (C.W.); xtzhang@nenu.edu.cn (X.Z.)

Abstract: Rational design of the surface of photocatalysts can conveniently modulate the photostimulated charge separation, influence the surface reaction kinetics, and other pivotal factors in the photocatalytic processes for efficient photocatalysis. Solution plasma, holding promise for mild modification of the surface structure of materials, has recently been recognized as an emerging technology for surface engineering of high-performance photocatalysts. In this review, we will briefly introduce the fundamentals of solution plasma and its applications in materials preparation and summarize the recent research progress in the surface design of advanced photocatalysts by solution plasma. Lastly, we will indicate some possible new directions. This review is expected to provide an instructive guideline for the surface design of heterogeneous photocatalysts by solution plasma.

Keywords: solution plasma; photocatalysts; surface structure design; single-atom metal; semiconductor oxides

check for updates

Citation: Wang, R.; Wang, C.; Xing, Y.; Zhang, X. Solution Plasma for Surface Design of Advanced Photocatalysts. *Catalysts* **2023**, *13*, 1124. https://doi.org/10.3390/catal13071124

Academic Editors: Detlef W. Bahnemann and Wenfeng Shangguan

Received: 26 June 2023
Revised: 13 July 2023
Accepted: 17 July 2023
Published: 19 July 2023

Copyright: © 2023 by the authors. Licensee MDPI, Basel, Switzerland. This article is an open access article distributed under the terms and conditions of the Creative Commons Attribution (CC BY) license (https://creativecommons.org/licenses/by/4.0/).

1. Introduction

The surface of photocatalysts, as the reaction site of the photocatalytic process, determines the efficiency and selectivity of photocatalysis [1–4]. The surface structure of photocatalysts, such as vacancies, heteroatoms, amorphousness, crystal facets, etc., essentially dominates surface electronic states [5–22] and then controls almost all factors in photocatalysis, including light absorption and charge separation of photocatalysts, adsorption of reactants, as well as the path and kinetics of surface reactions. Therefore, the surface design of photocatalysts is the core issue in photocatalysis, which has received continuous attention from researchers, thereby developing a variety of surface modification methods [23–46].

Plasma is an ionized system consisting of electrons, positive and negative ions, neutral or excited atoms and molecules, radicals, and photons [47]. Plasma generated in solution at normal temperature and pressure, that is, solution plasma (SP) [48], is regarded as a novel and unique technology in the surface modification of photocatalysts, taking advantage of multiple physical fields (electric fields, thermal fields, light fields, liquid annealing, etc.) involved and abundant active species with redox capacity (e_{aq}^-, ·H, ·OH, ·O, O_2^-, etc.). These can synergistically impact on the surface of photocatalysts for modification. More importantly, the high density and strong internal pressure of the solution environment lead to weaker kinetic energy of the plasma, which facilitates the gentle surface modification of photocatalysts without changing the bulk properties. Therefore, SP has attracted extensive attention in recent years as a powerful tool for the surface structure design of photocatalysts [49–57].

In this article, we will briefly introduce the fundamentals of SP, including the principles, the configurations of the experimental setup, the physiochemical properties of SP, and its applications in materials preparation. Then we will review the recent research progress in the surface design of advanced photocatalysts by SP. Lastly, we will suggest some new directions. This review is expected to provide an instructive guideline for the materials

science applications of the emerging SP technology, especially on the surface design of heterogeneous photocatalysts.

2. SP Fundamental

The SP installations can be divided into the following categories according to the type and position of the electrode, as shown in Figure 1. The reactors for plasma discharging in liquid mainly include rod-rod, needle-plate, wire-plate, and plate-hole (in an insulation plate)-plate types (Figure 1a–d). In addition, the gas-liquid plasma installations can be roughly divided into needle-plate, multi-needle-plate, and plate-plate types (Figure 1e–g). The configurations of the electrode generally affect plasma temperature, active species content, the characteristics of physical fields, and other parameters in SP, furthering the surface modification of photocatalysts, which has been systematically reviewed in the previous literature [58–60].

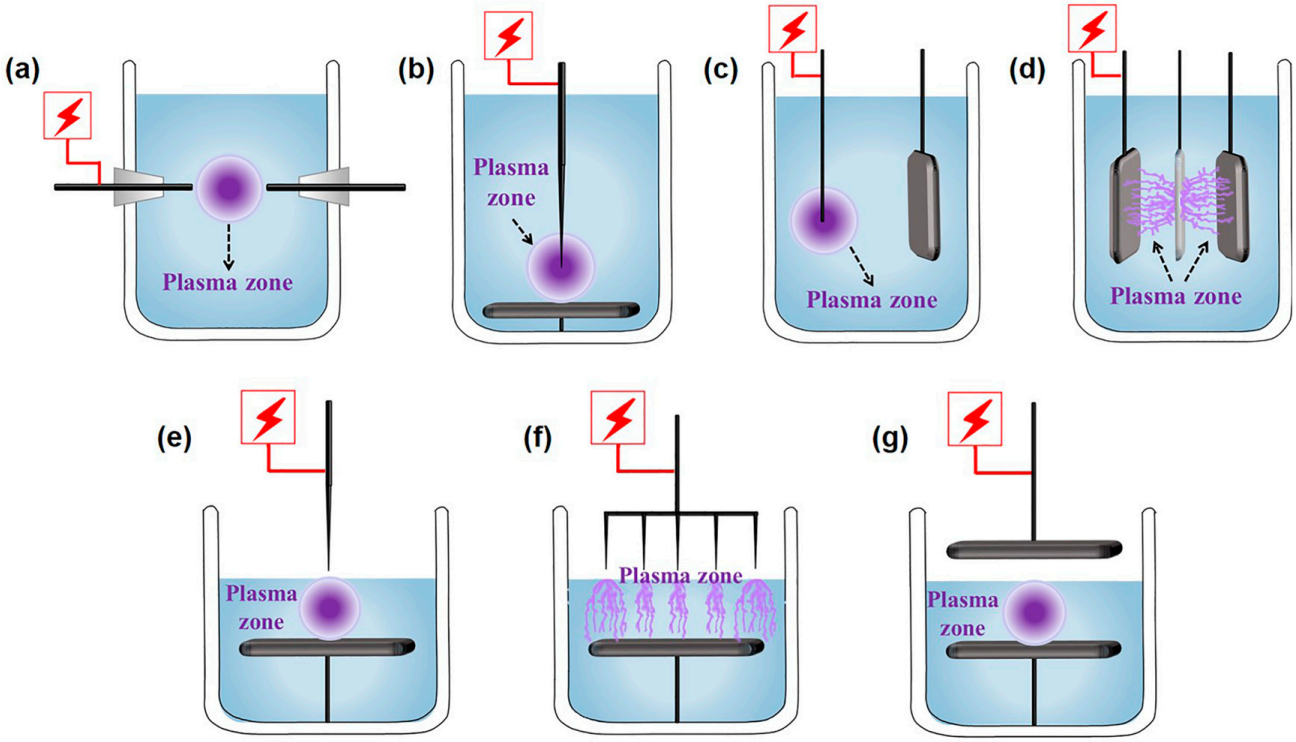


Figure 1. Schematic diagram of plasma discharging in the liquid phase form (**a**) rod-rod, (**b**) needle-plate, (**c**) wire-plate, and (**d**) plate-hole (in an insulation plate)-plate types. Schematic diagram of gas-liquid plasma discharge from (**e**) needle-plate, (**f**) multi-needle-plate, and (**g**) plate-plate types.

In this article, we focus on the rod-rod reactor, a typical configuration of in-liquid plasma, which has the advantages of simple construction, convenient operation, and a low ambient temperature. For generating plasma in liquid, specifically by applying a high voltage pulse to metal electrodes, bubbles around the electrode tip are created due to the local Joule heating effect [61,62]. When the applied energy exceeds a certain threshold in bubbles, an electric breakdown occurs, thereby forming a plasma. Subsequently, accompanied by the extension and expansion of plasma, a roughly circular discharge of plasma appears along the gas-liquid interface (Figure 2a). Bubbles are critical in plasma formation because they lower the threshold for electric breakdown [63]. In this regard, a series of gases, such as N_2, O_2, Ar, He, etc., are usually introduced into the solution to help plasma generation.

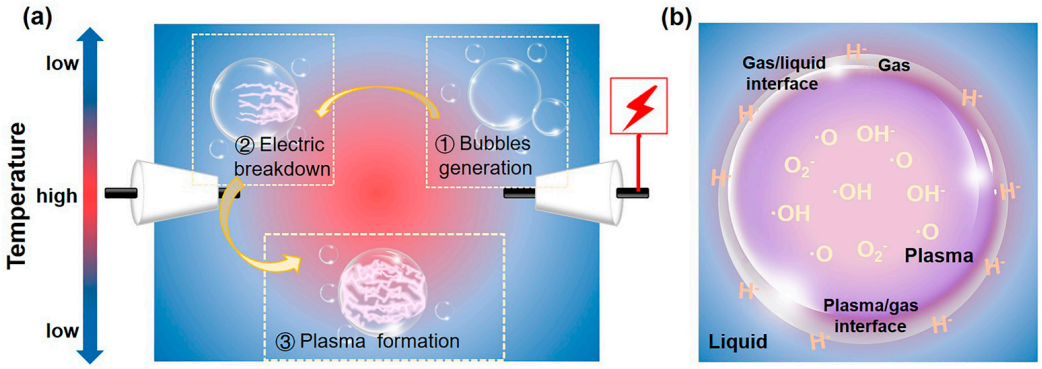


Figure 2. Schematic diagram of (**a**) the SP formation process and (**b**) the distribution of reaction sites and reactive species in SP.

2.1. Physical and Chemical Properties of SP

In the SP process, as shown in Figure 2b, reaction places involve the plasma phase, gas phase, liquid phase, plasma-gas interface, and gas-liquid interface. Among them, the plasma phase, liquid phase, and gas-liquid interface, with various physical and chemical effects, play a more significant role in the surface modification of photocatalysts [58].

In SP, the photoelectric effect and inelastic collision between high-energy electrons and surrounding molecules result in its ionization, excitation, and decomposition, which then generate various active species, such as e_{aq}^-, ·H, ·OH, ·O, O_2^-, H_2O^+, H_3O^+, H_2O_2, etc. The possible fundamental reactions in SP are summarized in Table 1. These active species with redox capacity are very important for the surface modification of photocatalysts. The density of plasma reaches 10^{17}–10^{20} cm^{-3} [64]. The active species differ in their spatial distribution. The ·OH, ·O, O_2^- and other oxygen-containing ions have a high mass, which causes slow migration speeds, finally remaining in plasma. Differently, ·H with a small mass can move quickly to the gas-liquid interface (Figure 2b) [65]. The optical emission spectrum (OES) is a useful method to detect free radicals and can offer effective information such as their composition and quantity [66]. Yu et al. utilized OES to investigate active radicals in water plasma (Figure 3a) [67]. They observed emission lines of H_α (3d → 2p: 656.6 nm), H_β (4d → 2p: 486.1 nm), and O_I (5p → $5s^0$: 777.5 nm; 3p → $3s^0$: 844.6 nm). Moreover, the electron density (N_e) was deduced from the full width at half-maximum (fwhm) of the H_β line, and the calculated formula was determined as $\text{fwhm} = 4.8 \times \left(N_e/10^{23}\right)^{0.68116}$ by Bratescu et al. [68].

Table 1. A brief summary of the possible fundamental reactions in SP.

No.	Reaction	No.	Reaction
1	$H_2O \rightarrow H_2O^*$	12	$e_{aq}^- + \bullet H + H_2O \rightarrow H_2 + OH^-$
2	$H_2O^* \rightarrow \bullet H + \bullet OH$	13	$e^- + O_2 \rightarrow O(^3P) + O(^1D) + e^-$
3	$H_2O^* \rightarrow H_2 + \bullet O$	14	$\bullet OH + H_2O_2 \rightarrow H_2O + \bullet HO_2$
4	$H_2O \rightarrow H_2O^+ + e^-$	15	$O(^1D) + H_2O \rightarrow 2\bullet OH$
5	$e^- + H_2O \rightarrow e_{aq}^-$	16	$\bullet H + O_2 \rightarrow \bullet O + \bullet OH$
6	$e^- + O_2 \rightarrow O_2^-$	17	$\bullet H + \bullet OH \rightarrow H_2O$
7	$H_2O + e^{-*} \rightarrow \bullet OH + \bullet H + e^-$	18	$\bullet OH + \bullet OH \rightarrow H_2O_2$
8	$H_2O + e^{*-} \rightarrow H_2O^+ + 2e^-$	19	$\bullet H + \bullet HO_2 \rightarrow H_2O_2$
9	$H_2O^+ + H_2O \rightarrow H_3O^+ + \bullet OH$	20	$\bullet H + \bullet H \rightarrow H_2$
10	$e_{aq}^- + \bullet OH \rightarrow OH^-$	21	$H_2O^+ + e_{aq}^- \rightarrow H_2O$
11	$e_{aq}^- + H_2O \rightarrow \bullet H + OH^-$		

* excited state; • radical; O_2^-: superoxide radical; $O(^3P)$: triplet oxygen; $O(^1D)$: singlet oxygen.

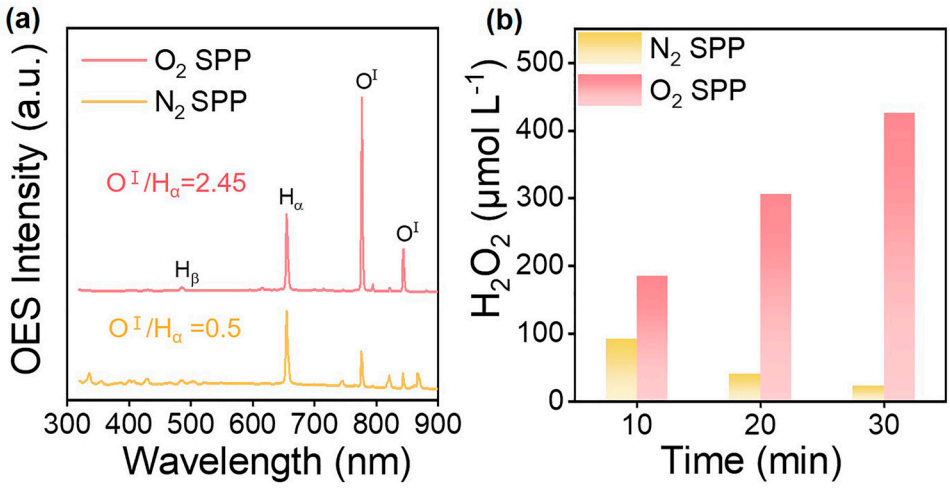


Figure 3. (**a**) Emission spectra of plasma discharging in water with N_2 or O_2; (**b**) the generation of H_2O_2 in SP with N_2 or O_2. Adapted with permission from Ref. [67]. Copyright © 2023 Elsevier B.V.

H radicals, with strong reducing abilities, are critical for the surface modification of photocatalysts and the generation of metal nanoparticles. Its density is easily affected by the SP configuration. In SP, bubbling inert gases (Ar, N_2, He, etc.) into solution can produce a higher concentration of the ·H radical. According to the reports from Sun et al. [69], the elastic collision of inert gas increased the average energy of electrons and then promoted the decomposition rate of water molecules for producing the ·H radical. The addition of alcohol in SP also plays a positive role in the ·H radical. Wang et al. found that the hydrogenation degree of P25-TiO_2 treated with alcohol plasma was stronger than that treated with water plasma [70]. Sudare et al. reported that adding alcohol to the $HAuCl_4$ solution increased the reduction rate of Au nanoparticles by SP [71]. Coherently, alcohol plasma exhibited a higher reduction rate of graphene oxide than reported by Takeuchi et al. [62]. This can be traced to the difference in the physical properties of alcohol and water. Compared with water, alcohol has a lower dielectric constant, which is conducive to trigger discharging [72]. The low boiling point and surface tension of alcohol induce denser and smaller bubbles [62], which fills the electrode gap, thereby leading to more sustained discharging. Besides, the C-H and O-H bond energies in alcohol are lower than the O-H bond energies in water [73] and are more likely to break in SP. Therefore, plasma discharging in alcohol can generate more ·H radicals for material preparation and modification. The electrode composition influences the discharge process. Miron et al. found that the Ta electrode system created fewer ·H radicals compared to the W electrode system [66]. Given that they reported the higher energy required for discharging breakdown in the Ta electrode system [66], the decrease in ·H radical was due to the poor discharging effect.

O species, including ·OH, ·O, O_2^-, and H_2O_2, are responsible for the synthesis of metal oxides and the surface structure design of photocatalysts. Yu et al. examined OES spectra in N_2- and O_2-bubbled SP and found that the concentration of O species in O_2-bubbled SP was enhanced by 4.9 times compared with N_2-bubbled SP (Figure 3a) [67]. In addition, the production of H_2O_2 in O_2-bubbled SP outweighed that in N_2-bubbled SP (Figure 3b) [67]. This manifested O_2 favored the formation of oxygen species. The main reason was that O_2 itself reacted with H atoms to form more ·O and ·OH radicals. Xing et al. observed that the enhanced oxygen species in O_2-bubbled SP tended to heal the surface oxygen vacancies (Ovs) of photocatalysts [74]. The conductivity and pH of the solution also affect the formation of the ·OH radicals. Sun et al. investigated the emission intensity of ·OH radical at different conductivities in KCl and KOH solutions [75]. Results indicated that when the conductivity ranged from 10 to 80 μS/cm, the concentration of the ·OH radical reached its maximum. Both too-low and too-high conductivity impeded discharging. Moreover, the concentration of ·OH radical in the KOH solution was higher than that in the KCl solution, suggesting that ·OH radical preferred neutral and slightly alkaline conditions.

Making use of a Cu electrode to discharge in water, Hayashi et al. found that sputtered Cu atoms might help accelerate the formation of the ·OH radical [76].

The temperature of the plasma region reaches 10^4–10^5 K [64], which is essential for material modification. The high-temperature region provides a pathway for the nucleation growth of metals, the phase transition of oxides, and the thermal decomposition, polymerization, and growth of organic precursors into carbon nanomaterials. On the other hand, the huge difference in temperature between the plasma phase and the liquid phase constitutes a unique physical process, i.e., solution annealing [70]. This process can freeze and retain the modified metastable structure. In addition, the instantaneous high temperature in the plasma region with the applied high voltage pulse makes the pressure in the discharging channel rise sharply. Then this causes the plasma channel to expand outward rapidly at a high speed (10^2~10^3 m/s) [77], forming a shock wave. The shock wave can act on the surface of materials to cause the crystal to break and rearrange.

In general, SP, as a novel material processing technology, integrates a variety of physical fields and chemical reactions. Its physicochemical effects can be conveniently adjusted by altering the plasma configurations, which provides great potential for surface structure modification of advanced materials.

2.2. SP for Materials Preparation

2.2.1. Oxide Materials

SP has been reported for the synthesis of semiconductor oxides with various physicochemical structures, such as vacancies, disordering, and foreign element doping. Pitchaimuthu et al. treated anatase-TiO_2 with water plasma in N_2 [78]. The surface amorphous layer and bulk brookite phase were created by being bombarded with high-energy ·H radicals. The crystal phase transformation and lattice rearrangement enhanced the yield of CO_2 from 50.9% to 96.6% in photocatalytic acetaldehyde degradation under ultraviolet light. Mizukoshi et al. prepared blue Ovs-TiO_2 by ammonia solution plasma [79]. Under visible light, the ·OH yield of SP-treated anatase-TiO_2 and P25-TiO_2 was higher than that of original TiO_2. This indicated that ammonia solution plasma enhanced the photooxidation capacity of anatase-TiO_2 and P25-TiO_2 under visible light. In addition to vacancies and amorphization, foreign element doping of materials has also been realized by SP. In a solution containing Ti sources and different F sources (Ti source: $TiOSO_4$ solution; F source: NaF, NaF with $[C_4MIM]HSO_4$, NaF with $[C_4MIM]BF_4$), plasma discharging synthesized F-doped anatase-TiO_2 [80]. The results showed that the addition of $[C_4MIM]HSO_4$ and $[C_4MIM]BF_4$ was conducive to the doping of F ions of NaF into the TiO_2 lattice. Moreover, the MB degradation rate of F-doped anatase-TiO_2 ($[C_4MIM]BF_4$ as an F doping agent) was improved by 2.9 times.

Besides, making use of the corresponding metal electrodes, plasma discharging in different electrolytes can be employed to prepare metal oxides with various morphologies. The black TiO_2 nanosphere was prepared by SP with a Ti electrode [81]. Additionally, it had a high specific surface area (~120 m^2 g^{-1}) and mesopore structure, which facilitated MB photodegradation. By replacing water with HNO_3 or KCl solution, the generated rate of black TiO_2 was enhanced, and in the HNO_3 solution, it reached the highest [82,83]. This was because of the high acidic property and conductivity of HNO_3. Kim et al. used coil-needle Zn electrodes in water plasma and synthesized bullet-like ZnO nanoparticles with the main exposed (100) crystal facet [84]. Saito et al. reported that plasma discharging with Zn electrodes prepared flower-like ZnO nanoparticles in a high-temperature and unstirred K_2CO_3 solution [85]. Table 2 summarizes various oxides prepared by SP in brief [78–89].

Table 2. A brief summary of various SP-prepared oxides.

Oxides			SP Conditions		Ref.
Samples	**Characteristics**	**Performance**	**Solution**	**Electrode**	
Anatase /Brookite TiO_2	surface amorphous layer, bulk brookite phase and oxygen defects	96.6% of CO_2 conversion rate in degradation of the gaseous acetaldehyde under a fluorescent lamp with 8000 lux intensity	water	W	[78]
Blue TiO_2	oxygen defects	105 µmol of H_2 generated in 2 h irradiated by a xenon lamp with 5 mW/cm^2	aqueous ammonia	W	[79]
Fluorine-doped TiO_2	anatase phase TiO_2 with interstitial fluorine atoms	~98% of MB degradation under stimulated sunlight for 30 min	$TiOSO_4$ solution with NaF, a mixed solution of NaF and $[C_4MIM]BF_4$, or a mixed solution of NaF and $[C_4MIM]HSO_4$	stainless steel	[80]
Black TiO_{2-x} spheres	a mixture of rutile, anatase, and oxygen-deficient TiO_2; disordered structure; oxygen defects and Ti^{3+}	90% of MB degradation under visible-light irradiation for 3 h	water	Ti	[81]
Black TiO_2	disordered structure and Ti^{3+}	58.49% of glycerol conversion under a 120W mercury lamp for 24 h	KCl or HNO_3	Ti	[82,83]
ZnO nanobullets	the main exposed (100) facet, and the (101) facet at the inclined surfaces in the edges	—	water	Zn	[84]
ZnO flowers	ZnO nanoflowers with a small number of Zn particles	100% of MB degradation under UV light irradiation for 120 min	K_2CO_3 solution	Zn	[85]
CuO nanorods	highly anisotropic CuO nanorods with 2–4 nm of diameter and 14–16 nm of length	—	$NaNO_3$ solution	Cu	[86]
Cu_2O	large particles with sizes of 300–500 nm	—	$NaNO_3$ solution and ascorbic acid	Cu	[86]
Nanoporous MnO_2	a spherelike shape; nanoparticles and thin layered structure	>99% of MB degradation for 2 min	$KMnO_4$ solution with glucose, fructose, or sucrose	W	[87]
WO_3 nanoparticles	monoclinic phase and an average particle diameter of ~60 nm	100% of RB degradation under UV irradiation for 50 min	HNO_3, NaOH, NaCl and glucose solution	W	[88]
ZnO nanospheres	nanospheres with about 17 nm in diameter	100% of MO degradation for 8 min under UV irradiation	$ZnCl_2$, KCl and $CO(NH_2)_2$ aqueous solution	W	[89]

2.2.2. Carbon Materials

Adopting organic solvents for discharging, SP can be employed to synthesize diversified advanced carbon materials. In SP, the bombardment of high-energy species and the thermolysis effect in the high-temperature plasma region can dissociate organic molecules into various unsaturated organic fragments. Subsequently, through heating integration in the plasma region and polymerization at the gas-liquid interface, various carbon materials can be synthesized. In 2013, Kang et al. prepared carbon nanospheres in a benzene solution for discharging [90]. Aromatic benzene with delocalized π electrons, which are considered to be easily excited by plasma, is rapidly decomposed to synthesize carbon materials in SP. As the applied frequency increased from 25 to 65 kHz, the carbon nanospheres grew from amorphous carbon to graphene. The reason was that the increase in frequency raised the temperature in the plasma region, exceeding the temperature critical point for nanocrystalline carbon formation. Recently, Romero Valenzuela et al. connected the SP reactor to an annealing chamber. Thus, SP-generated gaseous soot containing carbon seeds was blown by Ar to a nickel foil substrate in the annealing chamber, on which carbon fibers were grown at 400 °C in H_2/Ar [91]. Using benzene as the precursor, the SP-synthesized crude carbon nanofibers with a diameter of 150–220 nm were characteristic of a bumpy surface and random distribution. For dichlorobenzene, the SP-synthesized single fiber was grown in a columnar fashion and formed bundle structures ranging from 90 to 140 nm. This morphological difference was caused by the chlorine species of dichlorobenzene softening the surface of the Ni substrate and subsequently altering the nucleation mode of carbon nanofibers. In terms of ethanol and methanol, the SP-synthesized carbon materials displayed thin fiber clusters (diameters: <76 nm). The volatility of alcohols may be the reason for the small size of carbon fibers. Besides, as shown in Table 3, SP also prepared other carbon nanomaterials, such as graphite-like carbon polymer, carbon black, and carbon quantum dots [90–95]. Overall, the design of organic precursor structure (functional groups, physical properties, etc.) is the key to the preparation of target carbon materials by SP.

Table 3. A brief summary of various SP-synthesized carbon materials.

Samples	Characteristics	SP Conditions	Ref.
Carbon nanospheres	amorphous carbon nanoparticles (25 kHz), turbostratic carbon nanoparticles (65 kHz)	benzene; W electrodes; 1.3 kV, 2.0 μs and 25–65 kHz; 20 min	[90]
Carbon fibers	thick-bump fibers with a diameter of 150–220 nm; fiber bundles with a diameter of 90–140 nm; worm-like fibers with a diameter of 80–114 nm; thin fiber cluster with a diameter of <38 nm; flower-like fiber clusters with a diameter of 72–76 nm	benzene, o-dichlorobenzene, N-methylpyrrolidone, ethanol, or methanol; W electrodes; 5 kV, 20 kHz, and 1.0 μs; 15 min	[91]
Graphite-like and amorphous carbon	graphite-like carbon: a lamellar stack structure; amorphous carbon: turbostratic carbon surrounding by multi-layer fullerene-like carbon	tributyl borate; W electrodes; 1.5 kV, 100 kHz, and 0.5 μs; 60 min	[92]
Short carbon nanotubes	short carbon nanotubes of 100–400 nm in length	multi-wall carbon nanotubes in KCl solution; W electrodes; 450 V and 12 kHz; 30 min	[93]
Oxygen-containing nanocarbon	carbon particles with a diameter of 20 to 50 nm, the graphite-like layered structure	benzene and 1,4-dioxane; W electrodes; 20 kHz, 1 μs and 1.2–1.6 kV; 10 min	[94]
Fluorescent carbon dots	monocrystalline and semicrystalline	fructose, glucose, and sucrose; W electrodes; 20 kHz, and 0.9 μs; 20 min	[95]

Furthermore, by selecting organic precursors with heteroatoms (such as N, B, S, F, et al.), SP can help heteroatoms incorporate or co-incorporate into carbon materials. Plasma discharging in a solution of pyridine and boric acid prepared N/B co-doped nanocarbon, as reported by Lee et al. [96]. The formation of an uncoupled B-C-N bond altered the electronic structure of nanocarbon and formed new active sites for enhanced oxygen reduction reaction (ORR) performance. Li et al. chose pyridine and acrylonitrile as precursors, respectively, to synthesize graphitic-N and amino-N-doped nanocarbons with SP [97]. They found that graphitic-N bonds promoted the four-electron transfer of ORR, and amino-N bonds shifted the ORR onset potential to more positive values. Panomsuwan et al. conducted plasma discharging in a mixture of toluene and trifluorotoluene and obtained F-doped amorphous nanocarbons with enhanced electrocatalytic activity in ORR [98]. They suggested the promotion of catalytic performance was related to the ionic C-F and semi-ionic C-F bonds on the surface of nanocarbon. Moreover, P-doped carbon balls, graphitic N-doped graphene, B-doped carbon nanoparticles, B/F co-doped carbon nanoparticles, and others were also synthesized by SP [96–110]. As summarized in Table 4, by selecting suitable organic precursors and SP configurations, SP can flexibly and conveniently synthesize multiple types of advanced carbon materials.

Table 4. A brief summary of various SP-synthesized foreign element-doped carbon materials.

Samples	Doping Amount	SP Conditions	Ref.
Boron-carbon-nitrogen nanocarbon	N: 3.8 at% B: 1.2 at%	pyridine, boric acid; W electrodes; 2 kV, 0.5 μs and 100 kHz; 30 min	[96]
Graphitic-N and amino-N in nitrogen-doped carbon	N: 2.01 at%; 2.50 at%; 2.54 at%; 2.97 at%	anthracene, pyridine, acrylonitrile; W electrodes; 2.0 kV, 1.0 μs and 20 kHz; 20 min	[97]
Fluorine-doped carbon	F: 4.52 at%	toluene, trifluorotoluene; W electrodes; ~1.0 kV, 0.60 μs and 20 kHz; 20 min	[98]
Nitrogen-doped carbon nanoparticles	N: 4.78 at%; 1.33 at%	acrylonitrile; W electrodes; ~1.5 kV, 1.0 μs and 20 kHz; 30 min	[99]
Nitrogen-doped carbons	N: 0.58 at% 1.29 at% 1.36 at%	cyanobenzene, 2-cyanopyridine, cyanopyrazine; W electrodes; 1.2–1.5 kV, 0.80 μs and 20 kHz; 30 min	[100]
Graphitic nitrogen-doped graphene	N: 18.79 at%	benzene and N, N-dimethylformamide; W electrodes; 1.6 kV, 1.0 μs and 180 kHz; 15 min	[101]
Cationic nitrogen-doped graphene	N: 13.4 at%	1-ethyl-3-methylimidazolium dicyanamide, dimethylformamide; W electrodes; 2.0 kV, 200 kHz and 1.0 μs; 5 min	[102]
Phosphorus-doped carbon balls	P: 4 at%	triphenylphosphine; WC electrodes; 2.0 kV, 100 kHz and 1.0 μs; 10 min	[103]
Nitrogen-Doped Carbon Nanoparticle/Carbon Nanofiber Composite	N: 1.35 at%	a suspension of carbon nanofiber and 2-cyanopyridine; W electrodes; 20 kHz and 0.8 μs; 30 min	[104]
Boron-doped, and boron/fluorine co-doped carbon nanoparticles	B: 0.91 at%, F: 1.95 at%; B: 1.08 at%, F: 3.38 at%	toluene, 2,4,6-Triphenylboroxin, 2,4,6-Tris(4-fluorophenyl) boroxin, 2,4,6-Tris(3,4-difluorophenyl) boroxin, 2,4,6-Tris(3,4,5-trifluorophenyl) boroxin; W electrodes; 1.5 kV, 0.50 μs and 100 kHz; 20 min	[105]
Nitrogen-carbon nanosheets	N: 1.3 at%	N-methyl-2-pyrrolidone; W electrodes; 2.0 kV, 1.0 μs and 200 kHz; 5 min	[106]
Nitrogen-doped carbon nanoparticles	N: 0.58 at% 0.51 at% 0.39 at%	benzene, pyrazine; W electrodes; 1.5 kV, 1.0 μs and 20 kHz; 20 min	[107]

Table 4. *Cont.*

Samples	Doping Amount	SP Conditions	Ref.
Boron-doped carbon nanoparticles	B: 0.67 at%	benzene, triphenyl borate; W electrodes; 1.0 μs and 20 kHz; 20 min	[108]
Nitrogen-doped carbon nanoparticles	N: 1.94 at% 1.85 at%, 0.63 at%	benzonitrile, 2-cyanopyridine, cyanopyrazine; W electrodes; 0.80 μs and 20 kHz; 30 min	[109]
Nitrogen, Boron, or Phosphorus doped carbon; Nitrogen-Boron co-doped carbon; Nitrogen-Phosphorus co-doped carbon	—	benzene, pyridine, phenylboronic acid, phenylphosphonic acid; W electrodes	[110]

2.2.3. Metal Materials

The reducing radicals in SP, for example, the ·H radical, can reduce metal ions into metal particles of various types, sizes, and shapes. In 2008, Hieda et al. reported that $HAuCl_4$ solution plasma synthesized Au nanoparticles with triangular, pentagonal, and hexagonal shapes [111]. The higher applied voltage and lower $HAuCl_4$ concentration resulted in a size reduction and anisotropic shapes of Au nanoparticles. Then, Bratescu et al. further adjusted the pH value in $HAuCl_4$ solution plasma and controlled the size of Au nanoparticles [68]. As the pH value increased from 3 to 12, the size of Au nanoparticles decreased from ~10 nm to ~1–2 nm. Bratescu found that at a high pH value, the reduction potential of Au^0 nanoparticles decreased to ~0.60 eV. Meanwhile, the enriched negative ions (AuO^-, $AuOH^-$, and Au_2O^-) were absorbed on the Au surface to create a repulsive force among the Au nanoparticles. These prevented excessive agglomeration of Au nanoparticles. Besides, the addition of reducing solvent promoted the generation rate of metal particles in SP. Sudare et al. reported that when the molar fraction of ethanol was 0.089, the reduction rate of Au nanoparticles was improved by 35.2 times [71,112]. Under the action of plasma, ethanol molecules split into stable reducing ethanol free radicals ($\cdot CH(CH_3)OH$). As described in Section 2.1, ethanol facilitated plasma discharging and easily produced more ·H radicals. Other short-chain alcohols had the same effect [71]. Thus, plasma discharging in a metal salt solution can be employed to quickly prepare metal nanoparticles of various sizes and shapes.

Except for plasma discharging in a metal salt solution, the sputtering of the metal electrode surface in SP is also an effective means to prepare metal nanoparticles. During SP, the high-energy species in the plasma region continuously attack the metal electrode surface, resulting in the sputtering of metal ions. Then, metal ions nucleate and grow into metal particles. In 2012, Hu et al. utilized Au electrodes sputtering in liquid nitrogen and successfully prepared well-crystalline spherical Au clusters with a mean diameter of ~1.25 nm [113], which represented the characteristics of multiple twins and were near monodispersed. When two electrodes adopt different metal compositions, SP can be used to prepare bimetallic alloys. Zhang et al. adopted Pt and Pd electrodes for plasma sputtering in a solution of water and methanol to synthesize PtPd alloy nanoparticles with sizes ranging from 2 nm to 5 nm [114]. In their study, methanol played a role in inhibiting the aggregation of PtPd nanoparticles. Table 5 briefly summarizes SP-prepared metal materials [68,71,111,113–123].

Table 5. A brief summary of various metal materials prepared by SP.

Samples	Characteristics	Electrode	Precursor Solution	Ref.
Au	~50 nm, and hexagonal shape; ~10 nm, and triangular, pentagonal and hexagonal shapes	W	0.3 mM and 0.65 mM $HAuCl_4$	[111]
Au	PH = 12, 1~2 nm PH = 3, ~10 nm PH = 6, ~4 nm	Pt	$HAuCl_4 \cdot 3H_2O$, hexadecyltrimethylammonium chloride, and NaOH	[68]
Au	$\chi_{(ethanol)}$ = 0, ~32 nm $\chi_{(ethanol)}$ = 0.089, <10 nm $\chi_{(ethanol)}$ = 1.0, ~25 nm	W	$HAuCl_4 \cdot 3H_2O$, ethanol, methanol, 2-propanol	[71]
Au	TA = 0 mM, 56.6 ± 19 nm TA = 0.42 mM, 47.8 ± 17.8 nm TA = 1.25 mM, 21 ± 6.1 nm TA = 5 mM, 11.2 ± 4.1 nm	Cu	$HAuCl_4$ solution with L-cysteine, glucosamine, salicylic acid, or terephthalic acid, terephthalic acid (TA)	[115]
Ag/chitosan	spherical shape and a mean diameter of <20 nm	Graphite	$AgNO_3$ and chitosan solution	[116]
Ag/alginate	spherical shape and size range of 5–40 ± 2.0 nm	W	5 mM $AgNO_3$ and 0.3%(w/w) alginate solution	[117]
Au	spherical shape and the mean diameter of 1.25 ± 0.5 nm	Au	liquid nitrogen and pure water	[113]
Pd	the average size of ~2 nm	Pd	Ketjen Black aqueous solution	[118]
Au	the average particle diameters of 4.32 ± 0.85 nm, 3.54 ± 1.04 nm, and 2.87 ± 0.77 nm	Au	0.2%, 0.5%, and 0.9% sodium alginate aqueous solution	[119]
Sn	in pure water, ~5 nm Sn particles; in gelatin aqueous solution, Sn particles with a diameter of 40 to 400 nm	Sn	pure water or gelatin aqueous solution	[120]
PtAu	1.5 ± 1.0 nm clusters	Pt and Au	water or ethanol solution	[121]
PdAu	the average size of 2–5 nm	Pd and Au	Ketjen Black aqueous solution	[122]
CoNi	the size range of ~3–200 nm	Co and Ni	liquid nitrogen	[123]
PtPd	the size range of 2–5 nm	Pt and Pd	water and methanol solution	[114]

2.2.4. Composite Materials

SP with easily turned configurations can be employed to prepare composite materials with complex composition and/or morphology. The reported SP-prepared metal/oxide structures include Au/hollow fibrous TiO_2, Pt/ZnO, Ag/Co_3O_4, Au/coating TiO_2, etc. [124–129]. In these works, the SP-prepared metals are characterized by clusters. Additionally, there have been reports of a series of SP-prepared oxide/carbon structures, such as cubic Co_3O_4/reduced graphene, ZnO/carbon fiber, and TiO_x/carbon nanosheets [130–132]. In SP-prepared metal/carbon structures, except for metal particles dispersed on the surface of carbon materials [118,122], SP was also employed to synthesize a core-shell structure with a few layers of graphene as the shell and metal nanoparticles (Cu, Pt, PtAu, PtAg, and PtPd) as the core [133,134]. This core-shell structure was prepared by metal electrode sputtering in a dimethylformamide (DMF) solution. Aliphatic DMF without delocalized π electrons exhibited a low synthesis rate of carbon, and then it preferred to obtain layered graphene rather than carbon nanoparticles. Furthermore, the N and O atoms in the DMF structure formed terminal bonds, thereby terminating the growth of carbon. In SP, the monolayer carbon was first adsorbed on the metal surface, followed by the growth and crystallization of the carbon shell in the high-temperature plasma region. Table 6 provides a summary of a series of SP-prepared composite materials [118,122,124–127,130–134].

Table 6. A brief summary of various composite materials prepared by SP.

Samples	SP Conditions	Ref.
Au/hollow fibrous TiO_2	A solution of TiO_2 hollow fibrous power and adipic acid; Au electrodes; 2.0 μs and 15 kHz; 4 min	[124]
Pt/ZnO	Zn and Pt electrodes; 15–20 kHz and 1–2 μs	[125]
Ag/Co_3O_4	distilled water; Ag and Co electrodes; 0.9 kV, 2.0 μs and 20 kHz; 300 s	[126]
Au/coating TiO_2	A solution of TiO_2 particles and 0.01 M NaOH; Au electrodes; 400 V; 1 h	[127]
Co_3O_4/reduced graphene	A solution of $Co(NO_3)_2{\cdot}6H_2O$ and reduced graphene oxide; graphite as the anode, and Cu as the cathode; 190 V; 180 s	[130]
ZnO/carbon fiber	$ZnSO_4$ solution; a carbon fiber fabric as the negative electrode and a stainless-steel needle as the positive electrode; 1.5 kV	[131]
TiO_x/carbon nanosheets	Titanium tetraisopropoxide, distilled water, nitric acid, and ethanol; W electrodes; five capacitors in parallel with 0.1 μF capacitance, 100 times of discharging, the stored energy of 10–90 J per pulse in capacitor	[132]
Pd/Ketjen Black	Ketjen Black aqueous solution; Pd electrodes; 15–20 kHz and 1–2 μs	[118]
PdAu/Ketjen Black	Ketjen Black aqueous solution; Pd and Au electrodes; 15–20 kHz and 1–2 μs	[122]
a core-shell structure with graphene as shell and Cu nanoparticles as core	Dimethylformamide; Cu electrodes; 1.0 kV, 1.0 μs and 100, 200 kHz; 60 min	[133]
a core-shell structure with graphene as shell and metal nanoparticles (Pt, PtAu, PtAg or PtPd) as core	Dimethylformamide; Pt, Au, Ag, Pd electrodes; 1.0 μs and 30 kHz; 60 min	[134]

3. Surface Design of Advanced Photocatalysts by SP

SP is recognized as an effective means of engineering the surface structure of photocatalysts. A solution with a high internal pressure would induce a short mean free path of electrons and ions in SP [135] and then result in a low collision energy between SP-generated species and the surface of photocatalysts. This is conducive to mild and wet etching on the surface of photocatalysts. Furthermore, the dense solvent molecules in the solution would contribute to the weak kinetic energy of the plasma phase, which favors gently modifying surface structure. Besides, the high density and variety of active species provide a high rate and multiple angles of surface modification for photocatalysts [64]. Due to these merits, SP has great potential in the surface structure design of advanced photocatalysts.

3.1. Surface Modification of Semiconductor Oxides

3.1.1. Surface Electronic State Regulation

The surface electronic state is closely related to the light absorption and charge separation of photocatalysts, which can be facilely tuned by electron traps [1,2]. However, light absorption capacity and efficient charge separation generally have a trade-off relationship. Photocatalysts are mostly nanosized, and various traps are possibly present in the photocatalyst, resulting in the coexistence of shallow-energy-level and deep-energy-level electron traps [136–139]. The electron traps with shallow- and deep-energy levels would be beneficial to broaden light absorption from ultraviolet to visible, even near-infrared. Unfortunately, deep-energy-level electron traps serve as centers for charge recombination. Therefore, to promote efficient charge separation and ensure high light absorption ability, it is indispensable to engineer the electron traps by maintaining or introducing shallow-energy-level electron traps and eliminating deep-energy-level electron traps in the nanosized photocatalyst [2].

Yu et al. utilized the N_2 bubbled-SP to adjust the surface electronic state of as-synthesized rich-Ovs TiO_2-AB photocatalysts (a mixture of TiO_2 of anatase and TiO_2(B)

phases as shown in Figure 4a) [140]. Results indicated that SP helped to incorporate H heteroatoms into the TiO_2 lattice and created shallow-level traps above the deep level of Ovs, eventually achieving both visible photoabsorption capacity and high catalytic efficiency. The Ovs, located at 0.75–1.18 eV in the forbidden band [141], as visible absorption sites, were introduced to TiO_2-AB by hydrothermal synthesis. After SP, hydrogen species derived from plasma-induced water splitting were adsorbed or inserted into the surface lattice of rich-Ovs TiO_2-AB (Figure 4b) and generated shallow-level traps near the CBB with enhanced light absorption (Figure 4c), definitively supported by reversed double-beam photoacoustic spectroscopy (RDB-PAS) (Figure 4d). Surprisingly, the introduced shallow-level traps of H heteroatoms were below CBB and above the deep-level traps of Ovs. Therefore, with the help of external energy input, such as heat, trapped photogenerated electrons can be pulled out of the deep-level traps and transferred to the CBB through shallow-level traps (Figure 4e). This improved the utilized yield of photogenerated charges for enhanced photocatalysis. The results of photothermal catalysis of CO_2 conversion were exactly confirmed above the viewpoints. Under solar light, the photothermal catalysis of CO and CH_4 yield over SP-treated TiO_2-AB was respectively increased by 299.9 and 108.5 times compared to that over TiO_2-AB in photocatalysis (Figure 4f). Moreover, SP-treated TiO_2-AB displayed 3.51 μmol g^{-1} h^{-1} of CO yield and 1.16 μmol g^{-1} h^{-1} of CH_4 yield under visible light. Besides, they expanded the investigative oxides from TiO_2 to ZnO, WO_3, and Ta_2O_5. The SP-treated ZnO, WO_3, and Ta_2O_5 photocatalysts all exhibited an enhanced CO_2 production rate in photothermal acetaldehyde degradation, increasing by 3.4, 2.8, and 2.9 times, respectively. This indicated that SP was universal for semiconductor oxides. Therefore, SP can introduce H heteroatoms into the surface of photocatalysts and regulate the surface electronic states, thereby promoting catalytic activity.

Yu et al. further changed N_2 bubbles into O_2 bubbles in SP and treated commercial N-TiO_2 photocatalysts [67]. N-TiO_2 is the most classical visible light photocatalyst [142], and its energy level of N heteroatoms is located above the valence band top. Compared with N_2 bubbles, the O_2-bubbled SP introduced more H heteroatoms into the N-TiO_2 lattice (Figure 5a). Correspondingly, RDB-PAS spectra displayed the more shallow-level traps of H heteroatoms below the CBB (Figure 5b). In brief, O_2-bubbled SP is more favorable to introducing hydrogen dopants and forming shallow-level traps. Moreover, the more shallow-level traps would form more compact channels for smoothly and efficiently extracting trapped photogenerated electrons and then realizing efficient catalytic activity (Figure 5c). Coherently, the photothermal acetaldehyde mineralization rate of O_2 bubbles-treated N-TiO_2 was 82.69%, which was higher than that of N_2 bubbles-treated N-TiO_2 (61.47%) under visible light. In conclusion, SP is an effective means to regulate the surface electronic states of photocatalysts and can be flexibly controlled by altering the conditions of SP.

3.1.2. Crystal Facet Modulation

Different exposed crystal facets of polyhedral photocatalysts would separate redox sites for effective charge separation. For example, Pan et al. reported that anatase TiO_2 represented the discrete oxidation and reduction sites on its {0 0 1} and {1 0 1} facets [14]. Tan et al. found the oxidation site and reduction site of Cu_2O, respectively, were located on its {1 0 0} facet and {1 1 1} facet [15]. Domen et al. utilized the oxidation site—{1 1 0} facet and the reduction site—{1 0 0} facet of $SrTiO_3$ to realize efficient charge separation for photocatalysis [16]. Li et al. reported that, for monoclinic $BiVO_4$, the {1 1 0} facet was the oxidation site and the {0 1 0} facet was the reduction site [17]. Thus, modulating the exposed facet structure of photocatalysts is one of the useful means to achieve photogenerated charge separation and improve photoactivity.

In a recent work, Che et al. reported that SP can conduct defect engineering over the crystal facet of decahedral $BiVO_4$ and then improve its crystal facet-dependent photoactivity [143]. In this work, because of the abundant bulk defects brought by hydrothermal synthesis, the pristine as-synthesized decahedral $BiVO_4$ showed severe photogenerated

charge recombination, which caused poor facet-dependent photoactivity. As shown in Figure 6a, the deposited Pt nanoparticles and MnO_x nanosheets were randomly distributed on the {0 1 0} and {1 1 0} facets of pristine decahedral $BiVO_4$. In contrast, after SP treatment, the Pt nanoparticles and MnO_x nanosheets can be selectively and separately deposited on the {0 1 0} and {1 1 0} facets (Figure 6b). Moreover, the density and dispersion of {1 1 0} facet-deposited MnO_x nanosheets were significantly increased. Then, through a series of precise characterizations, they elucidated the mechanism by which SP enhanced facet-dependent photoactivity. From the positron annihilation spectroscopy (Figure 6c), SP-treated $BiVO_4$ showed a decreased lifetime component of τ1 and an increased lifetime component of τ2, which indicated a decrease in bulk defects and an increase in surface defects. Combined with the electron spin resonance (ESR) signal of metal vacancy at g = 1.994 (Figure 6d) and the decreased molar ratio of V/Bi in SP-treated $BiVO_4$ (from 1.119% to 1.044%), the created surface defects were confirmed as vanadium vacancies. The DFT calculation manifested the formation energy of vanadium vacancy on the {1 1 0} facet (6.56 eV) was smaller than that on the {0 1 0} facets (7.79 eV). This demonstrated vanadium vacancies were mainly distributed on the {1 1 0} facet, which coincided with the improved density and dispersion of deposited MnO_x nanosheets. Therefore, SP can minimize bulk defects and introduce {1 1 0} facet-located vanadium vacancies. Such defect engineering enhanced the separation efficiency of photogenerated charges at the {1 1 0}/{0 1 0} interface, sequentially increasing the crystal facet-dependent photoactivity. In the meantime, the SP-treated $BiVO_4$ exhibited a 1.5-times improvement in oxygen evolution rate from photocatalytic water oxidation referred to pristine $BiVO_4$ (Figure 6e). From the above, it can be seen that SP works well in crystal facet modulation and has potential for improving the crystal facet-dependent photoactivity of other photocatalysts.

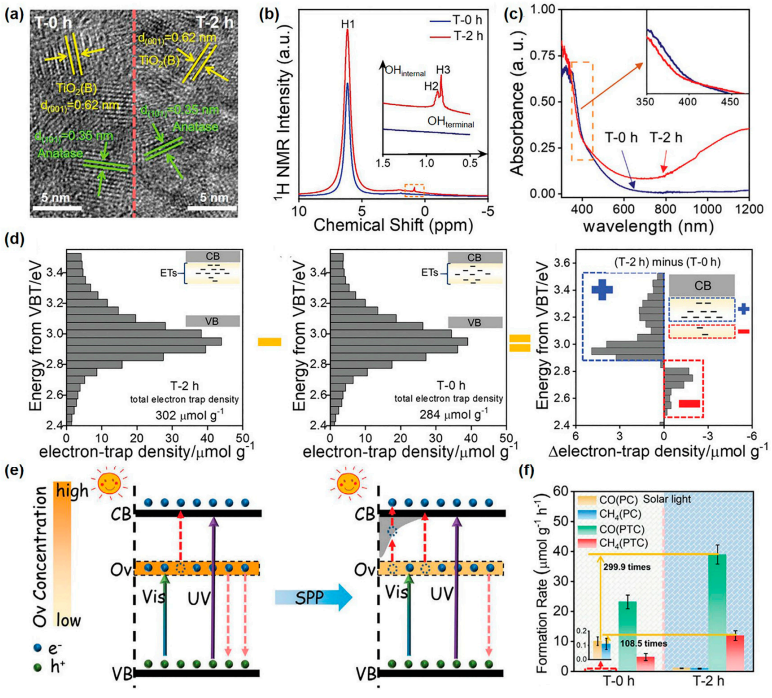


Figure 4. (**a**) High-resolution transmission electron microscope images (HRTEM); (**b**) solid ^1H nuclear magnetic resonance (^1H NMR) spectra; (**c**) ultraviolet-visible absorption spectra of TiO_2-AB and SP-treated TiO_2-AB samples. (**d**) from left to right, RDB-PAS spectra of SP-treated TiO_2-AB, TiO_2-AB, and the difference value of electron trap density between SP-treated TiO_2-AB and TiO_2-AB. (**e**) Schematic illustration of the electron–hole separation mechanism for TiO_2-AB and SP-treated TiO_2-AB during photocatalysis. (**f**) Photo- and photothermal CO_2 conversion rates over TiO_2-AB and SP-treated TiO_2-AB samples under solar light irradiation of 100 mW/cm^2. Adapted with permission from Ref. [140].

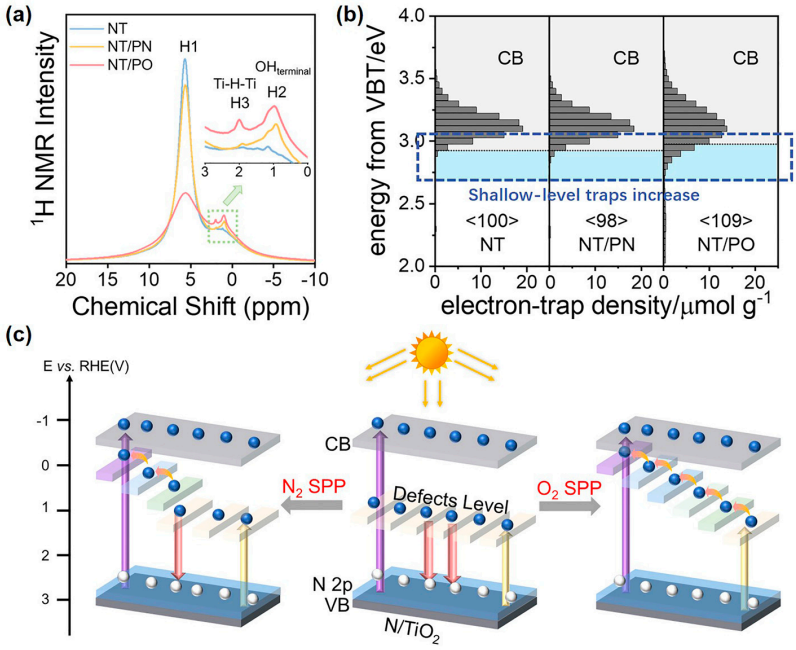


Figure 5. (**a**) ^{1}H NMR spectra; (**b**) RDB-PAS spectra; and (**c**) a schematic diagram of photoexcited electron transfer of N-TiO_2, N_2-bubbled SP-treated N-TiO_2, and O_2-bubbled SP-treated N-TiO_2. Adapted with permission from Ref. [67]. Copyright © 2023 Elsevier B.V.

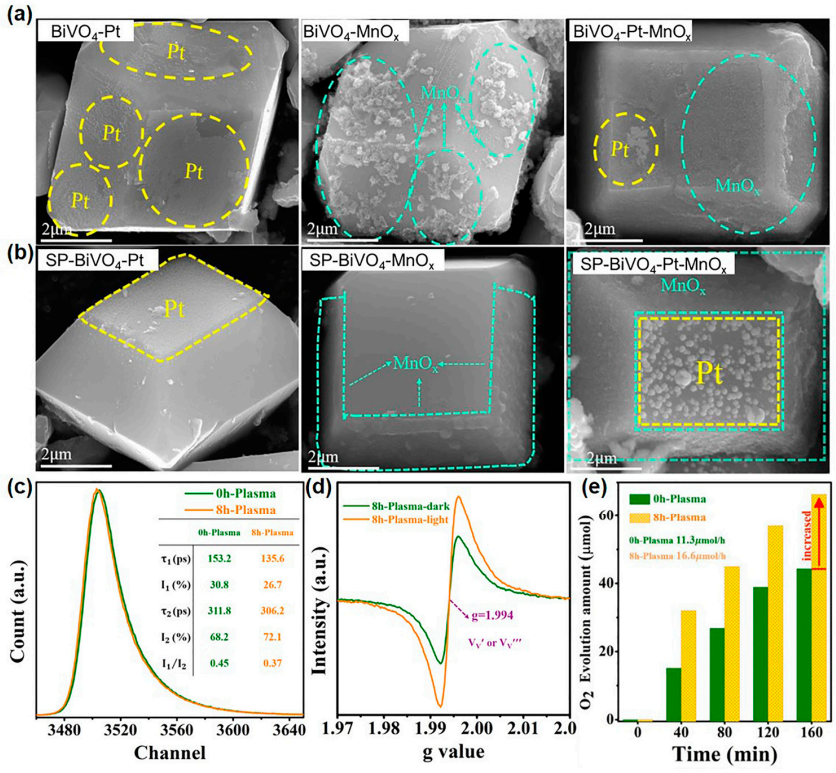


Figure 6. (**a**) From left to right, scanning electron microscopy (SEM) images of the Pt-loaded $BiVO_4$, the MnO_x-loaded $BiVO_4$, and the Pt/MnO_x-loaded $BiVO_4$. (**b**) From left to right, SEM images of the Pt-loaded SP-treated $BiVO_4$, the MnO_x-loaded SP-treated $BiVO_4$, and the Pt/MnO_x-loaded SP-treated $BiVO_4$. (**c**) Positron annihilation lifetime spectra of $BiVO_4$ and SP-treated $BiVO_4$. (**d**) ESR signal of SP-treated $BiVO_4$. (**e**) Photocatalytic oxygen evolution rate form water over $BiVO_4$ and SP-treated $BiVO_4$. The electron sacrificial agent was $AgNO_3$, and the light source was visible light ($\lambda \geq 420$ nm). Adapted from Ref. [143].

3.1.3. Surface Amorphization

A surface-amorphous TiO_2 catalyst was first reported by Chen et al. [144]. They reported that surface amorphization induced the CB and VB band-tail electronic states to narrow the bandgap of TiO_2 to ~1.54 eV, which then enhanced the photocatalytic activity of hydrogen evolution. Subsequently, Yang et al. constructed a heterojunction of TiO_2 and amorphous WO_3 nanoparticles [145]. They found the decoration of amorphous WO_3 allowed a rapid electron transfer to adsorbed O_2. Interestingly, the TiO_2-crystalline WO_3 heterojunction showed no electron transfer tendency, due to the fact that the CBB of crystalline WO_3 was lower than the reduction potential of O_2. They suggested the CBB of amorphous WO_3 may move up, exceeding the reduction potential of O_2. Moreover, Ohtani et al. recently observed that surface amorphization of TiO_2 caused a slight uplift of the CBB [146–148]. Therefore, amorphous oxides may favor the photocatalytic reduction reaction, and regretfully, this remains ambiguous.

Wang et al. utilized alcohol plasma to successfully introduce a thin amorphous layer (~0.7 nm) on the surface of commercial P25 (Figure 7a) [70]. The subsequent characterizations confirmed that the surface amorphous layer would passivate surface Ovs and raise the energy level of electron traps for enhanced separation and reduction capacity of photogenerated charges. As shown in Figure 7b, alcohol-plasma-treated P25 displayed a marked decrease in the ESR signal of g = 2.004 assigned to Ovs. Then, they investigated the distribution of Ovs by electron energy loss spectroscopy (EELS). For pristine P25, the Ti-$L_{2,3}$ edges collected in the surface region obviously shifted to the lower energy (Figure 7c), which illustrated that Ovs were mainly located on the surface. Disparately, the Ti-$L_{2,3}$ edges of alcohol-plasma-treated P25 barely shifted with a scan from the bulk to the surface (Figure 7d). These manifested Ovs are evenly distributed in alcohol-plasma-treated P25. Therefore, combined with HRTEM and ESR, the surface amorphous layer passivated the surface Ovs for alcohol-plasma-treated P25. Correspondingly, the RDB-PAS spectra of alcohol-plasma-treated P25 visually showed that the density of electron traps decreased. Furthermore, the energy level of electron traps was simultaneously uplifted (Figure 7e). This verified that the electron-donating ability of alcohol-plasma-treated P25 was improved, which was attributed to the surface amorphization of P25. This contributed to facilitating photocatalytic reduction. From the photocatalytic evolution of hydrogen under simulated solar irradiation, the hydrogen evolution rate of alcohol-plasma-treated P25 (1.982 mmol g^{-1} h^{-1}) was improved by 124 times compared with P25 (0.016 mmol g^{-1} h^{-1}) (Figure 7f). The apparent quantum efficiency (AQE) of it loaded with 0.3 wt% Pt reached 37.37% at 365 nm (Figure 7g). In addition, alcohol-plasma-treated anatase- and rutile-TiO_2 also exhibited structural and catalytic performance trends consistent with P25. This demonstration of alcohol plasma was generally applicable to other oxides. Moreover, compared with water-plasma-treated TiO_2 samples, alcohol plasma was superior in activating TiO_2.

The formation of the surface amorphous layer was closely related to the solution annealing. In their work, the alcohol solution split into H•, OH•, and $CH(CH_3)$ OH• radicals under the action of plasma. When P25 was added, the ESR signal intensity of H• and OH• radicals was obviously weakened. This result indicated that H• and OH• species interacted with the surface of P25 to result in surface amorphization. The above processes tended to be carried out in a high-temperature plasma region. Subsequently, under stirring, a dramatic quenching of modified P25 in a low-temperature liquid phase led to the freezing of the surface amorphous structure. To sum up, SP can efficiently realize the surface amorphization of semiconductor oxide with improved photocatalytic reduction performance, which is expected to be popularized by a variety of catalysts.

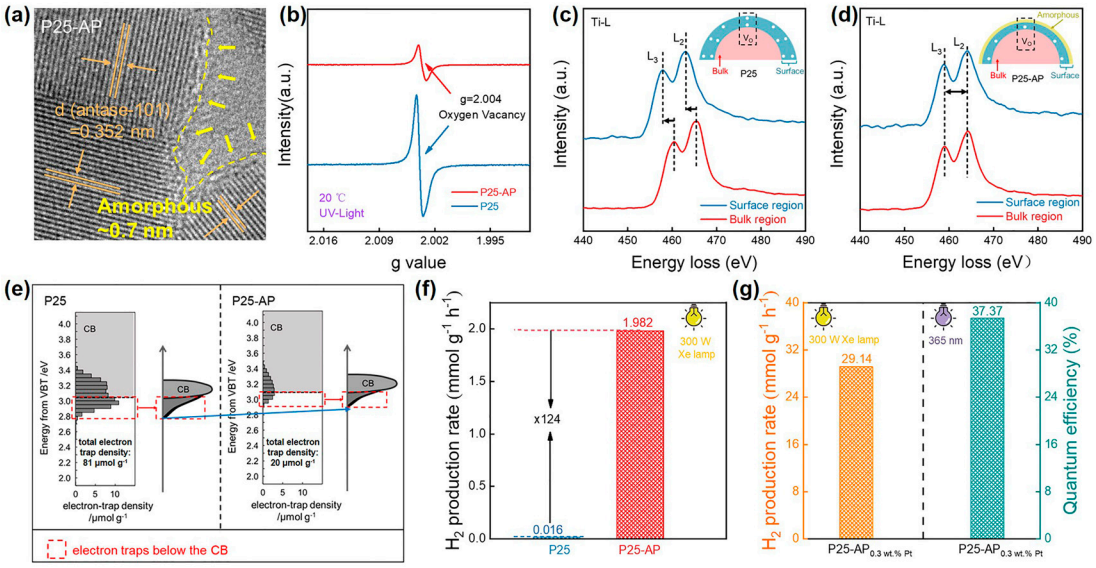


Figure 7. (**a**) HRTEM images of alcohol-plasma-treated P25; (**b**) ESR spectra; (**c**,**d**) EELS spectra of Ti-$L_{2,3}$; (**e**) RDB-PAS spectroscopy; (**f**) Photocatalytic hydrogen evolution rate of P25 and alcohol-plasma-treated P25. (**g**) Photocatalytic hydrogen evolution rate and AQE of alcohol-plasma-treated P25 located with 0.3 wt% Pt. Methanol was the sacrificial reagent, and the light sources were a 300 W Xe lamp and a 300 W Xe lamp with a 365 nm filter. Adapted with permission from Ref. [70]. Copyright © 2022 American Chemical Society.

3.2. Single-Atom Metal Synthesis and Support Modulation

As summarized in Table 5, the metal particles prepared by SP often display the characteristics of clusters. Compared with metal clusters, single-atom metals have a higher utilization rate of atoms, stronger metal-support interaction, and a unique electronic structure for excellent catalytic performance [149,150]. However, the high surface free energy of single-atom metals results in their easy aggregation to form clusters [151,152].

Recently, Xing et al. first utilized the N_2-bubbled SP to load single-atom Au on oxygen-deficient CeO_2 nanosheets within a short period of 2 min [74]. In their work, SP constructed Ovs on ultrathin and multiporous 2D CeO_2 nanosheets (Figure 8a), which acted as anchoring sites for single-atom Au. Thus, the synchronously SP-reduced Au in solution was rapidly and dispersedly captured on the surface of CeO_2 nanosheets in the form of a single atom (Figure 8b). For the synthesis of Au_1/CeO_2, the construction of Ovs on CeO_2 was a decisive factor. The reason was that by changing N_2 bubbles into O_2 bubbles in SP, Xing et al. found that Ovs were decreased, and then Au atoms were agglomerated into clusters (Figure 8c). In terms of SP-prepared Au_1/CeO_2, the Au L_3-edge X-ray absorption near edge structure (XANES) spectra displayed a higher intensity of the white line peak than Au foil (Figure 8d). This indicated the SP-prepared Au_1/CeO_2 was mainly composed of ionic $Au^{\delta+}$ species. Besides, the radial distance space spectrum $\chi(R)$ of SP-prepared Au_1/CeO_2 exhibited two distinct peaks located at ~1.97 and 2.87 Å, assigned to the scattering path of Au-O bonds, and assuredly no Au-Au scattering (Figure 8e). These results further confirmed that the loaded Au existed as a single atom and was coordinated with the O atom in CeO_2 nanosheets.

The SP-prepared Au_1/CeO_2 displayed prominent photopromoted low-temperature CO oxidation performance with a remarkable catalytic temperature decrease of ~100 °C. In the photocatalytic temperature-dependent CO oxidation experiment under solar light irradiation, the CO conversion over Au_1/CeO_2 was as high as 91.7% at 25 °C (Figure 8f). While in the dark, the lowest temperature to achieve 90% CO conversion required 125 °C (Figure 8f). These indicated that light helped enhance the catalytic activity. Xing et al. next selected a 375 nm laser as the light source because it avoided the introduction of photoinduced heat. Results indicated that the value of n, rooted in the sublinear relationship

as CO_2-yiled rate∝light intensity^n, was 0.72 (Figure 8g), which meant the reaction was a photodriven process. Therefore, the high CO oxidation activity over Au_1/CeO_2 under solar irradiation was dominated by the photoexcitation process. Furthermore, the reaction mechanism of the photodriven CO oxidation over Au_1/CeO_2 was adequately surveyed to be the MvK mechanism. By labeling Au_1/CeO_2 with ^{18}O, the mass spectra detected a signal of $^{18}O^{13}C^{16}O$ (Figure 8h), which indicated lattice oxygen in $Ce^{18}O_2$ support reacted with reactant CO. This was an important feature of the MvK mechanism. Therefore, the process of photodriven CO oxidation over Au_1/CeO_2 can be described as follows (Figure 8i). Reactant CO adsorbed at the single-atom Au site reacted with activated surface lattice oxygen to produce CO_2, simultaneously forming Ovs. Afterward, O_2 was adsorbed on the Ovs site to form the O_2^- anion and then dissociated into the O atom, refilling the Ovs.

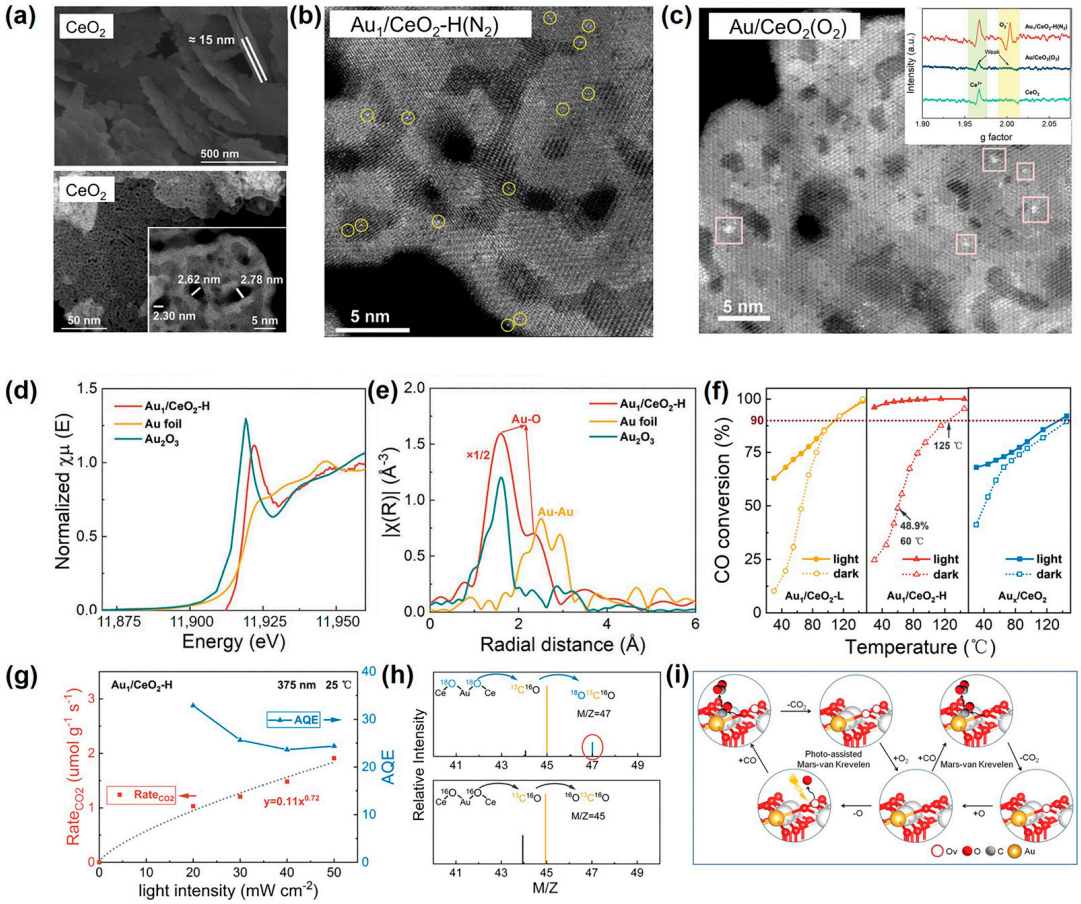


Figure 8. (**a**) From top to bottom, the SEM image and high-angle annular dark-filed scanning transmission electron microscopy (HAADF-STEM) images of CeO_2. (**b**) the HAADF-STEM images of Au_1/CeO_2-H(N_2). (**c**) the HAADF-STEM images of Au/CeO_2(O_2). Inset were the ESR spectra of CeO_2, Au/CeO_2(O_2), and Au_1/CeO_2-H(N_2); (**d**) Normalized Au L_3-edge XANES spectra and (**e**) Fourier transform EXAFS functions of Au_1/CeO_2-H. (**f**) The temperature dependence of CO conversion for Au_1/CeO_2 under light and in the dark. (**g**) The increment of Au_1/CeO_2-H in CO_2 production rate and corresponding AQE under a 375 nm laser at different light intensities. (**h**) Mass spectra of products obtained by the oxidation of ^{13}CO over Au_1/CeO_2-H. (**i**) Schematic diagram of the photo-enhanced MvK mechanism over the Au_1/CeO_2. Adapted with permission from Ref. [74]. Copyright © 2022 Wiley-VCH GmbH.

SP is a general approach to preparing other single-atom or double-atom metals. Xing et al. then successfully obtained Pd_1/CeO_2, Rh_1/CeO_2, AuPd/CeO_2, and AuRh/CeO_2 photocatalysts, and they all displayed the highlighted photocatalytic performance in the water gas shift reaction [74]. Moreover, they combined peristaltic pumps with the SP reactor

to achieve rapid continuous-flow preparation of single-atom metal, which contributed to the large-scale production [153]. In conclusion, SP has great research potential in the fabrication of single-atom metals, double-atom metals, multiple-atom metals, and even high-entropy alloys for various valuable catalytic reactions.

3.3. Construction of Multidimensional Heterojunctions

In addition to the single-atom metal, the photocatalyst surface can be embellished with SP-prepared carbon materials by changing the precursor solution into an organic solution in SP. Huang et al. recently reported that alcohol plasma modulated the defects of 2D ultrathin HNb_3O_8 nanosheets and synchronously anchored carbon dots (CDs) on the surface of HNb_3O_8 nanosheets in situ [154]. In this work, they found that plasma discharging in an ethanol solution can produce typical CDs with a lattice spacing of 0.24 nm. With the presence of 2D HNb_3O_8 nanosheets, the SP-produced carbon dots were dispersedly and tightly anchored to the surface of the HNb_3O_8 nanosheets to form a 0D/2D HNb_3O_8/C heterojunction, as shown in the HRTEM images in Figure 9a,b. The Raman spectra of the HNb_3O_8/C heterojunction detected two new peaks assigned to the D-band and G-band of CDs (Figure 9c), which again confirmed the decoration of HNb_3O_8 by CDs. Besides, both the O1s XPS peaks and the Nb 3d XPS peaks displayed an obvious shift to higher binding energy in the HNb_3O_8/C heterojunction (Figure 9d,e). These results manifested electron transfers from HNb_3O_8 to CDs at the interface of the HNb_3O_8/C heterojunction. Thus, the decoration of CDs on HNb_3O_8 enhanced the separation of charges. Besides, the HNb_3O_8/C heterojunction revealed the upshifted fermi energy level (E_f) and the downshifted valence band. The upward shift of E_f should result from the generation of shallow energy-level traps of hydrogen dopants. Additionally, the downward shift of the valence band may be caused by the passivation of defect states in pristine HNb_3O_8 nanosheets. Such defect modulation enhanced the redox capacity of charges. Therefore, the accelerated charge separation by CDs and defect modulation synergistically boosted the photocatalytic performance over the 2D HNb_3O_8 nanosheets. As shown in Figure 9f, the H_2 evolution rate over the HNb_3O_8/C heterojunction was 317.7 times higher than that over pristine HNb_3O_8 nanosheets. In addition, CDs, the mixture of CDs and untreated HNb_3O_8 nanosheets, and water-plasma-treated HNb_3O_8 nanosheets all showed much lower photocatalytic H_2 evolution performance compared with HNb_3O_8/C heterojunction. It proved that CD decoration and defect modulation were the pivotal reasons for the enhanced catalytic activity of the HNb_3O_8 nanosheets.

In addition to the HNb_3O_8/C heterojunction, SP also performed well in constructing other CDs/2D-layered transition metal oxoacid heterojunctions. For example, Huang et al. successfully fabricated the H_4TiO_4/C heterojunction by treating titanate nanosheets with alcohol plasma [154]. Besides ethanol, solution discharging with propanol and butanol also produced CDs [154]. This manifested SP can regulate the surface structure and simultaneously construct the heterojunction structure for advanced photocatalysts.

In conclusion, SP can modify the surface structure of photocatalysts and then regulate the crystal facet-dependent photoactivity and surface electronic states for efficient photocatalysts. Meanwhile, with the replacement of solutions, SP can synthesize single-atom metals, double-atom metals, and CDs as surface additives for photocatalysts. More interestingly, vacancies, amorphous phases, and others created by SP would have a positive impact on the morphology, dispersity, and electronic structure of additives to optimize photocatalysts for high-performance photocatalysis.

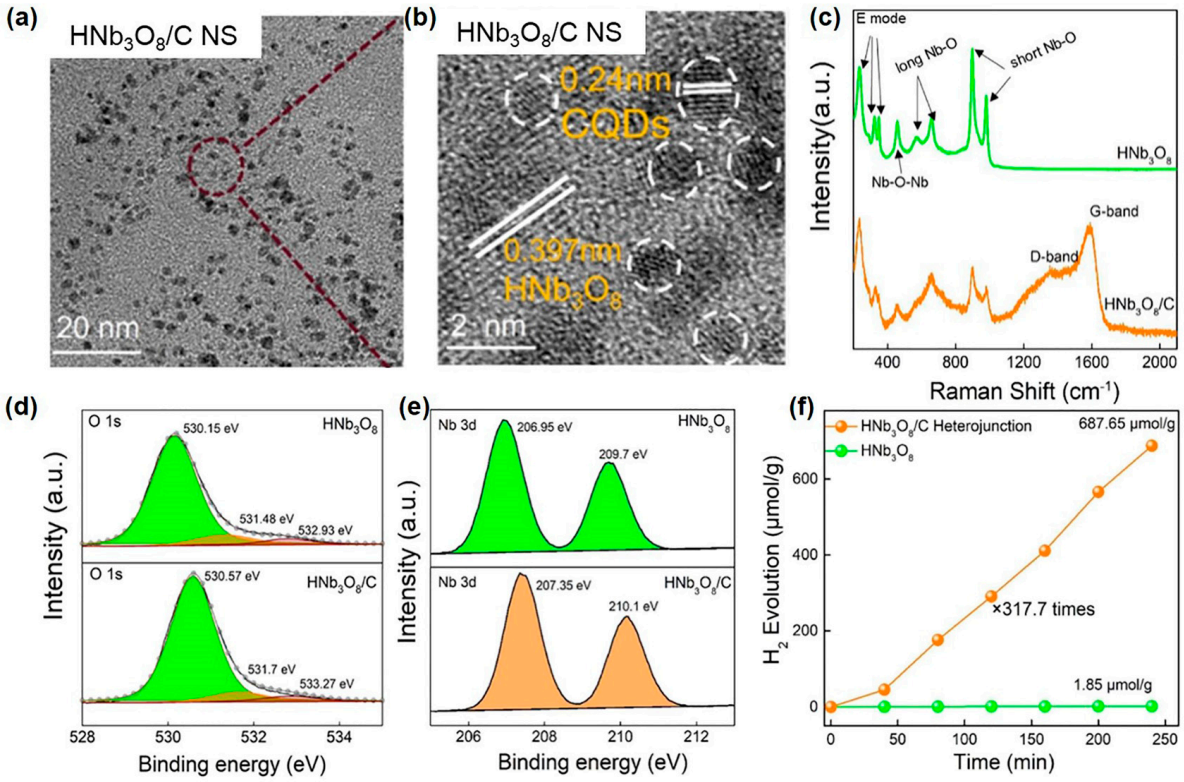


Figure 9. (**a**) TEM and (**b**) HRTEM images of the HNb_3O_8/C heterojunction; (**c**) Raman spectra; (**d**) and (**e**) X-ray photoelectron spectroscopy (XPS) spectra of HNb_3O_8 and HNb_3O_8/C heterojunction. (**f**) Photocatalytic hydrogen evolution rate of HNb_3O_8 and HNb_3O_8/C heterojunctions. The light source was a 300 W Xe lamp. Adapted with permission from Ref. [154]. Copyright © 2022 American Chemical Society.

4. Conclusions and Future Perspectives

In summary, the green, safe, and efficient SP has exhibited great advantages for the surface structure design of advanced photocatalysts. Its rich chemical active species and a variety of physical fields can synergistically act on the surface of photocatalysts for surface designs. At present, SP has been applied for surface electron state regulation, surface amorphization, crystal facet modulation, and additive decoration of photocatalysts. The physicochemical structure of SP-modified photocatalysts can be easily regulated by altering installation parameters (voltage, frequency, pulse width, reactor type, etc.) and the discharging environment (bubble species, electrode compositions, precursor solution, etc.). On the whole, SP has achieved a series of advanced progress in the surface modulation of photocatalysts, as shown in Figure 10.

Based on the numerous reported achievements of SP so far, we briefly discuss the challenges and opportunities for the SP field in the coming years, as follows:

I. The material systems are expanded from photocatalysis to electrocatalysis, thermal catalysis, dye-sensitized solar cells, etc. Recently, Li et al. utilized SP to modify transparent MoO_x film, loading it with Pt to act as counter electrodes for bifacial dye-sensitized solar cells (DSSCs). The fabricated DSSCs exhibited excellent double-sided electrocatalytic efficiency of 7.56% and 6.41% with front- and rear-side illumination, respectively [155]. Therefore, SP has the potential to prepare diversified materials for various fields. In addition, it is reasonably expected that the materials suitable for SP processing can be extended from oxides to sulfides, carbides, nitrides, etc., and even polymer systems, such as covalent-organic frameworks, metal-organic frameworks, porous organic polymers, etc.

II. SP has been successfully employed to prepare single-atom metals and double-atom metals for catalyst applications. It is reasonable to expect that multi-atom metal catalysts of metal kinds over three as well as high-entropy alloy catalysts could be prepared by SP in the future. In addition, non-metallic materials with the advantages of low cost and abundant reserves also have broad application prospects. SP can be attempted to synthesize non-metallic single atoms, non-metallic multiple atoms, and even non-metallic high-entropy alloys.

III. Plasma catalysis has achieved a series of achievements in nitrogen fixation, waste degradation, and fuel synthesis [156–158]. The combination of SP with various types of catalysis, such as photo-, thermal-, and electro-catalysis, may possibly achieve rapid mass production and directional selection of products with low energy consumption. Extra energy input can accelerate the reaction rate for mass production. Moreover, different energy fields may affect the proportion of active species and alter the catalytic reaction paths, ultimately achieving precise product orientation.

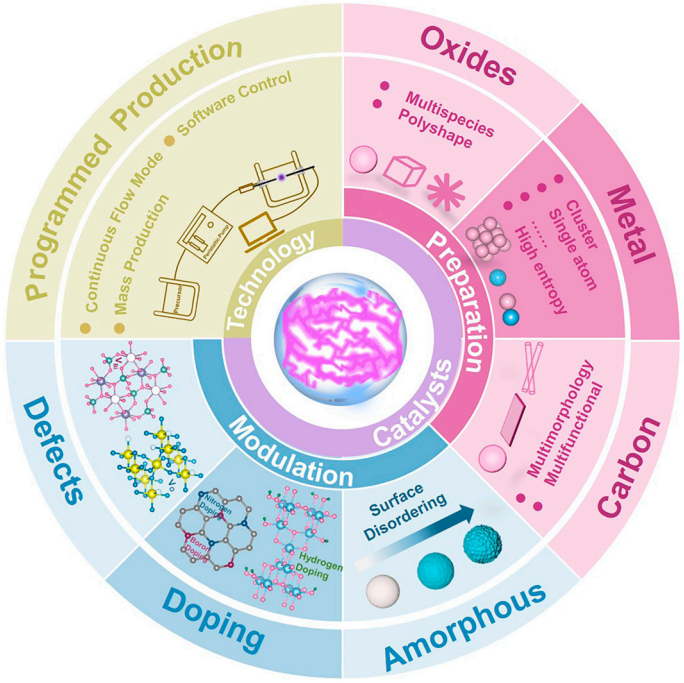


Figure 10. A concise summary diagram of SP-modified/prepared photocatalysts.

Author Contributions: Conceptualization, X.Z.; writing—original draft preparation, R.W.; data curation, R.W.; visualization, R.W.; writing—review and editing, Y.X., C.W. and X.Z.; supervision, C.W. and X.Z.; project administration, and funding acquisition, X.Z. All authors have read and agreed to the published version of the manuscript.

Funding: This research and the APC were funded by the National Natural Science Foundation of China (grant nos. 52273236, U22A2078, 51872044 and 91833303), Jilin Province Science and Technology Development Project (grant no. 20220201073GX).

Data Availability Statement: Not applicable.

Conflicts of Interest: The authors declare no conflict of interest.

References

1. Fujishima, A.; Zhang, X.T.; Tryk, D.A. TiO_2 photocatalysis and related surface phenomena. *Surf. Sci. Rep.* **2008**, *63*, 515–582. [CrossRef]
2. Ohtani, B. Titania Photocatalysis beyond Recombination: A Critical Review. *Catalysts* **2013**, *3*, 942–953. [CrossRef]

3. Fujishima, A.; Honda, K. Electrochemical photolysis of water at a semiconductor electrode. *Nature* **1972**, *238*, 37–38. [CrossRef] [PubMed]
4. Roy, N.; Suzuki, N.; Terashima, C.; Fujishima, A. Recent Improvements in the Production of Solar Fuels: From CO_2 Reduction to Water Splitting and Artificial Photosynthesis. *Bull. Chem. Soc. Jpn.* **2019**, *92*, 178–192. [CrossRef]
5. Kong, L.N.; Wang, C.H.; Wan, F.X.; Zheng, H.; Zhang, X.T. Synergistic effect of surface self-doping and Fe species-grafting for enhanced photocatalytic activity of TiO_2 under visible-light. *Appl. Surf. Sci.* **2017**, *396*, 26–35. [CrossRef]
6. Kong, L.N.; Jiang, Z.Q.; Wang, C.H.; Wan, F.X.; Li, Y.Y.; Wu, L.Z.; Zhi, J.-F.; Zhang, X.T.; Chen, S.J.; Liu, Y.C. Simple ethanol impregnation treatment can enhance photocatalytic activity of TiO_2 nanoparticles under visible-light irradiation. *ACS Appl. Mater. Interfaces* **2015**, *7*, 7752–7758. [CrossRef]
7. Hu, Y.; Li, X.B.; Wang, W.W.; Deng, F.; Han, L.; Gao, X.M.; Feng, Z.J.; Chen, Z.; Huang, J.T.; Zengi, F.Y.; et al. Bi and S Co-doping g-C_3N_4 to Enhance Internal Electric Field for Robust Photocatalytic Degradation and H_2 Production. *Chin. J. Struct. Chem.* **2022**, *41*, 2206069–2206078.
8. Li, Y.Y.; Wang, C.H.; Zheng, H.; Wan, F.X.; Yu, F.; Zhang, X.T.; Liu, Y.C. Surface oxygen vacancies on WO_3 contributed to enhanced photothermo-synergistic effect. *Appl. Surf. Sci.* **2017**, *391*, 654–661. [CrossRef]
9. Wang, D.; Zhang, X.T.; Sun, P.P.; Lu, S.; Wang, L.L.; Wang, C.H.; Liu, Y.C. Photoelectrochemical water splitting with rutile TiO_2 nanowires array: Synergistic effect of hydrogen treatment and surface modification with anatase nanoparticles. *Electrochim. Acta* **2014**, *130*, 290–295. [CrossRef]
10. Jiang, T.T.; Xie, W.W.; Geng, S.P.; Li, R.C.; Song, S.Q.; Wang, Y. Constructing oxygen vacancy-regulated cobalt molybdate nanoflakes for efficient oxygen evolution reaction catalysis. *Chin. J. Catal.* **2022**, *43*, 2434–2442. [CrossRef]
11. Shen, R.C.; Hao, L.; Chen, Q.; Zheng, Q.Q.; Zhang, P.; Li, X. P-Doped g-C_3N_4 Nanosheets with Highly Dispersed $Co_{0.2}Ni_{1.6}Fe_{0.2}P$ Cocatalyst for Efficient Photocatalytic Hydrogen Evolution. *Acta Phys.-Chim. Sin.* **2022**, *38*, 2110014.
12. Zheng, H.; Wang, C.H.; Zhang, X.T.; Li, Y.Y.; Ma, H.; Liu, Y.C. Control over energy level match in Keggin polyoxometallate-TiO_2 microspheres for multielectron photocatalytic reactions. *Appl. Catal. B* **2018**, *234*, 79–89. [CrossRef]
13. Wang, C.H.; Zhang, X.T.; Liu, Y.C. Coexistence of an anatase/TiO_2(B) heterojunction and an exposed (001) facet in TiO_2 nanoribbon photocatalysts synthesized via a fluorine-free route and topotactic transformation. *Nanoscale* **2014**, *6*, 5329–5337. [CrossRef] [PubMed]
14. Pan, J.; Liu, G.; Lu, G.Q.; Cheng, H.M. On the true photoreactivity order of {001}, {010}, and {101} facets of anatase TiO_2 crystals. *Angew. Chem. Int. Ed.* **2011**, *50*, 2133–2137. [CrossRef]
15. Tan, C.S.; Hsu, S.C.; Ke, W.H.; Chen, L.J.; Huang, M.H. Facet-Dependent electrical conductivity properties of Cu_2O crystals. *Nano Lett.* **2015**, *15*, 2155–2160. [CrossRef]
16. Takata, T.; Jiang, J.Z.; Sakata, Y.; Nakabayashi, M.; Shibata, N.; Nandal, V.; Seki, K.; Hisatomi, T.; Domen, K. Photocatalytic water splitting with a quantum efficiency of almost unity. *Nature* **2020**, *581*, 411–414. [CrossRef]
17. Li, R.G.; Zhang, F.X.; Wang, D.G.; Yang, J.X.; Li, M.R.; Zhu, J.; Zhou, X.; Han, H.X.; Li, C. Spatial separation of photogenerated electrons and holes among {010} and {110} crystal facets of $BiVO_4$. *Nat. Commun.* **2013**, *4*, 1432. [CrossRef]
18. Khan, T.T.; Bari, G.A.K.M.R.; Kang, H.-J.; Lee, T.-G.; Park, J.-W.; Hwang, H.-J.; Hossain, S.M.; Mun, J.S.; Suzuki, N.; Fujishima, A.; et al. Synthesis of N-Doped TiO_2 for Efficient Photocatalytic Degradation of Atmospheric NO_x. *Catalysts* **2021**, *11*, 109. [CrossRef]
19. Wang, C.H.; Zhang, X.T.; Zhang, Y.L.; Jia, Y.; Yuan, B.; Yang, J.K.; Sun, P.P.; Liu, Y.C. Morphologically-tunable TiO_2 nanorod film with high energy facets: Green synthesis, growth mechanism and photocatalytic activity. *Nanoscale* **2012**, *4*, 5023–5030. [CrossRef]
20. Hunge, Y.M.; Uchida, A.; Tominaga, Y.; Fujii, Y.; Yadav, A.A.; Kang, S.-W.; Suzuki, N.; Shitanda, I.; Kondo, T.; Itagaki, M.; et al. Visible Light-Assisted Photocatalysis Using Spherical-Shaped $BiVO_4$ Photocatalyst. *Catalysts* **2021**, *11*, 460. [CrossRef]
21. Wang, C.H.; Zhang, X.T.; Zhang, Y.L.; Jia, Y.; Yang, J.K.; Sun, P.P.; Liu, Y.C. Hydrothermal Growth of Layered Titanate Nanosheet Arrays on Titanium Foil and Their Topotactic Transformation to Heterostructured TiO_2 Photocatalysts. *J. Phys. Chem. C* **2011**, *115*, 22276–22285. [CrossRef]
22. Kim, J.-H.; Hossain, S.M.; Kang, H.-J.; Park, H.; Tijing, L.; Park, G.W.; Suzuki, N.; Fujishima, A.; Jun, Y.-S.; Shon, H.K.; et al. Hydrophilic/Hydrophobic Silane Grafting on TiO_2 Nanoparticles: Photocatalytic Paint for Atmospheric Cleaning. *Catalysts* **2021**, *11*, 193. [CrossRef]
23. Takeshi, M.; Ryoji, A.; Takeshi, O. 11-Nitrogen Doping into TiO_2 and Loading of Co-Catalysts for Enhanced Photocatalysis Under Visible-Light Irradiation. In *Handbook of Self-Cleaning Surfaces and Materials From Fundamentals to Applications*; Fujishima, A., Irie, H., Zhang, X.T., Tryk, D.A., Eds.; Wiley-VCH GmbH: Weinheim, Germany, 2023; pp. 264–271.
24. Yu, F.; Wang, C.H.; Ma, H.; Song, M.; Li, D.S.; Li, Y.Y.; Li, S.M.; Zhang, X.T.; Liu, Y.C. Revisiting Pt/TiO_2 photocatalysts for thermally assisted photocatalytic reduction of CO_2. *Nanoscale* **2020**, *12*, 7000–7010. [CrossRef] [PubMed]
25. Li, Y.Y.; Wang, C.H.; Song, M.; Li, D.S.; Zhang, X.T.; Liu, Y.C. TiO_{2-x}/CoO_x photocatalyst sparkles in photothermocatalytic reduction of CO_2 with H_2O steam. *Appl. Catal. B* **2019**, *243*, 760–770. [CrossRef]
26. Lu, S.; Wang, Y.L.; Li, F.; Yang, G.C.; Yang, H.Y.; Zhang, X.T.; Liu, Y.C. Adsorption Energy Optimization of Co_3O_4 through Rapid Surface Sulfurization for Efficient Counter Electrode in Dye-Sensitized Solar Cells. *J. Phys. Chem. C* **2017**, *121*, 12524–12530. [CrossRef]

27. Wang, J.J.; Meeprasert, J.; Han, Z.; Wang, H.; Feng, Z.D.; Tang, C.Z.; Sha, F.; Tang, S.; Li, G.N.; Pidko, E.A.; et al. Highly dispersed Cd cluster supported on TiO_2 as an efficient catalyst for CO_2 hydrogenation to methanol. *Chin. J. Catal.* **2022**, *43*, 761–770. [CrossRef]
28. Ding, X.M.; Liang, Y.L.; Zhang, H.L.; Zhao, M.; Wang, J.L.; Chen, Y.Q. Preparation of Reduced Pt-Based Catalysts with High Dispersion and Their Catalytic Performances for NO Oxidation. *Acta Phys.-Chim. Sin.* **2022**, *38*, 2005009. [CrossRef]
29. Kong, L.N.; Zhang, X.T.; Wang, C.H.; Wan, F.X.; Li, L. Synergic effects of Cu_xO electron transfer co-catalyst and valence band edge control over TiO_2 for efficient visible-light photocatalysis. *Chin. J. Catal.* **2017**, *38*, 2120–2131. [CrossRef]
30. Zheng, H.; Wang, C.H.; Zhang, X.T.; Kong, L.N.; Li, Y.Y.; Liu, Y.Y.; Liu, Y.C. Ultrasonic spray pyrolysis assembly of a TiO_2-WO_3-Pt multi-heterojunction microsphere photocatalyst using highly crystalline WO_3 nanosheets: Less is better. *New J. Chem.* **2016**, *40*, 3225–3232. [CrossRef]
31. Yan, J.Y.; Wang, C.H.; Ma, H.; Li, Y.Y.; Liu, Y.C.; Suzuki, N.; Terashima, C.; Fujishima, A.; Zhang, X.T. Photothermal synergic enhancement of direct Z-scheme behavior of $Bi_4TaO_8Cl/W_{18}O_{49}$ heterostructure for CO_2 reduction. *Appl. Catal. B* **2020**, *268*, 118401. [CrossRef]
32. Li, C.M.; Chen, K.; Wang, X.Y.; Xue, N.; Yang, H.Q. Understanding the Role of Cu/ZnO Interaction in CO_2 Hydrogenation to Methanol. *Acta Phys.-Chim. Sin.* **2021**, *37*, 2009101.
33. Yang, Y.; Wu, J.S.; Cheng, B.; Zhang, L.Y.; Al-Ghamdi, A.A.; Wageh, S.; Li, Y.J. Enhanced Photocatalytic H_2-production Activity of CdS Nanoflower using Single Atom Pt and Graphene Quantum Dot as Dual Cocatalysts. *Chin. J. Struct. Chem.* **2022**, *41*, 2206006–2206014.
34. Li, S.M.; Wang, C.H.; Li, D.S.; Xing, Y.M.; Zhang, X.T.; Liu, Y.C. Bi_4TaO_8Cl/Bi heterojunction enables high-selectivity photothermal catalytic conversion of CO_2-H_2O flow to liquid alcohol. *Chem. Eng. J.* **2022**, *435*, 135133. [CrossRef]
35. Zhang, M.M.; Wang, C.H.; Wang, Y.Y.; Li, S.M.; Zhang, X.T.; Liu, Y.C. Tunable bismuth doping/loading endows $NaTaO_3$ nanosheet highly selective photothermal reduction of CO_2. *Nano Res.* **2023**, *16*, 2142–2151. [CrossRef]
36. Zhang, Y.; Wang, D.; Zhang, X.T.; Chen, Y.; Kong, L.N.; Chen, P.; Wang, Y.L.; Wang, C.H.; Wang, L.L.; Liu, Y.C. Enhanced photoelectrochemical performance of nanoporous $BiVO_4$ photoanode by combining surface deposited cobalt-phosphate with hydrogenation treatment. *Electrochim. Acta* **2016**, *195*, 51–58. [CrossRef]
37. Peng, X.F.; Wang, C.H.; Li, Y.Y.; Ma, H.; Yu, F.; Che, G.S.; Yan, J.Y.; Zhang, X.T.; Liu, Y.C. Revisiting cocatalyst/TiO_2 photocatalyst in blue light photothermalcatalysis. *Catal. Today* **2019**, *335*, 286–293. [CrossRef]
38. Zhou, X.M. TiO_2-Supported Single-Atom Catalysts for Photocatalytic Reactions. *Acta Phys.-Chim. Sin.* **2021**, *37*, 2008064.
39. Wang, Z.P.; Lin, Z.P.; Shen, S.J.; Zhong, W.W.; Cao, S.W. Advances in designing heterojunction photocatalytic materials. *Chin. J. Catal.* **2021**, *42*, 710–730. [CrossRef]
40. Wang, C.H.; Zhang, X.T.; Yuan, B.; Wang, Y.X.; Sun, P.P.; Wang, D.; Wei, Y.G.; Liu, Y.C. Multi-heterojunction photocatalysts based on WO_3 nanorods: Structural design and optimization for enhanced photocatalytic activity under visible light. *Chem. Eng. J.* **2014**, *237*, 29–37. [CrossRef]
41. Mao, G.B.; Wu, H.; Qiu, T.Y.; Bao, D.J.; Lai, L.J.; Tu, W.G.; Liu, Q. WO_3@Fe_2O_3 Core-Shell Heterojunction Photoanodes for Efficient Photoelectrochemical Water Splitting. *Chin. J. Struct. Chem.* **2022**, *41*, 2208025–2208030.
42. Luo, X.; Zhu, Z.; Tian, Y.; You, J.; Jiang, L. Titanium Dioxide Derived Materials with Superwettability. *Catalysts* **2021**, *11*, 425. [CrossRef]
43. Wan, F.X.; Kong, L.N.; Wang, C.H.; Li, Y.Y.; Liu, Y.C.; Zhang, X.T. The W@WO_3 ohmic contact induces a high-efficiency photooxidation performance. *Dalton Trans.* **2017**, *46*, 1487–1494. [CrossRef]
44. Wang, C.H.; Zhang, X.T. Anatase/Bronze TiO_2 Heterojunction: Enhanced Photocatalysis and Prospect in Photothermal Catalysis. *Chem. Res. Chin. Univ.* **2020**, *36*, 992–999. [CrossRef]
45. Tamboli, A.H.; Suzuki, N.; Terashima, C.; Gosavi, S.; Kim, H.; Fujishima, A. Direct Dimethyl Carbonates Synthesis over CeO_2 and Evaluation of Catalyst Morphology Role in Catalytic Performance. *Catalysts* **2021**, *11*, 223. [CrossRef]
46. Sridharan, K.; Shenoy, S.; Kumar, S.G.; Terashima, C.; Fujishima, A.; Pitchaimuthu, S. Advanced Two-Dimensional Heterojunction Photocatalysts of Stoichiometric and Non-Stoichiometric Bismuth Oxyhalides with Graphitic Carbon Nitride for Sustainable Energy and Environmental Applications. *Catalysts* **2021**, *11*, 426. [CrossRef]
47. Neyts, E.C. Plasma-Surface Interactions in Plasma Catalysis. *Plasma Chem. Plasma Process.* **2016**, *36*, 185–212. [CrossRef]
48. Horikoshi, S.; Serpone, N. In-liquid plasma: A novel tool in the fabrication of nanomaterials and in the treatment of wastewaters. *RSC Adv.* **2017**, *7*, 47196. [CrossRef]
49. Takai, O. Fundamentals and Applications of Solution Plasma. *J. Photopolym. Sci. Technol.* **2014**, *27*, 379–384. [CrossRef]
50. Terashima, C.; Iwai, Y.; Cho, S.P.; Ueno, T.; Zettsu, N.; Saito, N.; Takai, O. Solution Plasma Sputtering Processes for the Synthesis of PtAu/C Catalysts for Li-Air Batteries. *Int. J. Electrochem. Sci.* **2013**, *8*, 5407–5420. [CrossRef]
51. Terashima, C.; Arihara, K.; Okazaki, S.; Shichi, T.; Tryk, D.A.; Shirafuji, T.; Saito, N.; Takai, O.; Fujishima, A. Fabrication of Vertically Aligned Diamond Whiskers from Highly Boron-Doped Diamond by Oxygen Plasma Etching. *ACS Appl. Mater. Interfaces* **2011**, *3*, 177–182. [CrossRef]
52. Terashima, C.; Hishinuma, R.; Roy, N.; Sugiyama, Y.; Latthe, S.S.; Nakata, K.; Kondo, T.; Yuasa, M.; Fujishima, A. Charge Separation in TiO_2/BDD Heterojunction Thin Film for Enhanced Photoelectrochemical Performance. *ACS Appl. Mater. Interfaces* **2016**, *8*, 1583–1588. [CrossRef] [PubMed]

53. Harada, Y.; Hishinuma, R.; Spataru, N.; Sakurai, Y.; Miyasaka, K.; Terashima, C.; Uetsuka, H.; Suzuki, N.; Fujishima, A.; Kondo, T.; et al. High-speed synthesis of heavily boron-doped diamond films by in-liquid microwave plasma CVD. *Diamond Relat. Mater.* **2019**, *92*, 41–46. [CrossRef]
54. Hirami, Y.; Hunge, Y.M.; Suzuki, N.; Rodriguez-Gonzalez, V.; Kondo, T.; Yuasa, M.; Fujishima, A.; Teshima, K.; Terashima, C. Enhanced degradation of ibuprofen using a combined treatment of plasma and Fenton reactions. *J. Colloid Interface Sci.* **2023**, *642*, 829–836. [CrossRef] [PubMed]
55. Mizoi, K.; Rodriguez-Gonzalez, V.; Sasaki, M.; Suzuki, S.; Honda, K.; Ishida, N.; Suzuki, N.; Kuchitsu, K.; Kondo, T.; Yuasa, M.; et al. Interactions between pH, reactive species, and cells in plasma-activated water can remove algae. *RSC Adv.* **2022**, *12*, 7626–7634. [CrossRef] [PubMed]
56. Gosavi, S.; Tabei, R.; Roy, N.; Latthe, S.S.; Hunge, Y.M.; Suzuki, N.; Kondo, T.; Yuasa, M.; Teshima, K.; Fujishima, A.; et al. Low Temperature Deposition of TiO_2 Thin Films through Atmospheric Pressure Plasma Jet Processing. *Catalysts* **2021**, *11*, 91. [CrossRef]
57. Prasertsung, I.; Damrongsakkul, S.; Terashima, C.; Saito, N.; Takai, O. Preparation of low molecular weight chitosan using solution plasma system. *Carbohydr. Polym.* **2012**, *87*, 2745–2749. [CrossRef]
58. Chokradjaroen, C.; Wang, X.; Niu, J.; Fan, T.; Saito, N. Fundamentals of solution plasma for advanced materials synthesis. *Mater. Today Adv.* **2022**, *14*, 100244. [CrossRef]
59. Saito, G.; Akiyama, T. Nanomaterial Synthesis Using Plasma Generation in Liquid. *J. Nanomater.* **2015**, *2015*, 123696. [CrossRef]
60. Vanraes, P.; Bogaerts, A. Plasma physics of liquids—A focused review. *Appl. Phys. Rev.* **2018**, *5*, 031103. [CrossRef]
61. Saito, N.; Bratescu, M.A.; Hashimi, K. Solution plasma: A new reaction field for nanomaterials synthesis. *Jpn. J. Appl. Phys.* **2018**, *57*, 0102A4. [CrossRef]
62. Takeuchi, N.; Kawahara, K.; Gamou, F.; Li, O.L.H. Observation of solution plasma in water–ethanol mixed solution for reduction of graphene oxide. *Int. J. Plasma Environ. Sci. Technol.* **2020**, *14*, e01009.
63. Averin, K.A.; Bilera, I.V.; Lebedev, Y.A.; Shakhatov, V.A.; Epstein, I.L. Microwave discharge in liquid n-heptane with and without bubble flow of argon. *Plasma Process. Polym.* **2019**, *16*, e1800198. [CrossRef]
64. Namihira, T.; Sakai, S.; Yamaguchi, T.; Yamamoto, K.; Yamada, C.; Kiyan, T.; Sakugawa, T.; Katsuki, S.; Akiyama, H. Electron temperature and electron density of underwater pulsed discharge plasma produced by solid-state pulsed-power generator. *IEEE Trans. Plasma Sci.* **2007**, *35*, 614–618. [CrossRef]
65. Chen, Q.; Kaneko, T.; Matsuda, N.; Hatakeyama, R. Potential structure of discharge plasma inside liquid directly measured by an electrostatic probe. *Appl. Phys. Lett.* **2013**, *102*, 244105. [CrossRef]
66. Miron, C.; Bratescu, M.A.; Saito, N.; Takai, O. Time-resolved Optical Emission Spectroscopy in Water Electrical Discharges. *Plasma Chem. Plasma Process.* **2010**, *30*, 619–631. [CrossRef]
67. Yu, F.; Wang, C.H.; Wang, R.; Li, Y.H.; Ohtani, B.; Fujishima, A.; Zhang, X.T. Solution plasma engineering the surface of nitrogen doped TiO_2 for photothermal catalysis. *Appl. Surf. Sci.* **2023**, *624*, 157119. [CrossRef]
68. Bratescu, M.A.; Cho, S.-P.; Takai, O.; Saito, N. Size-Controlled Gold Nanoparticles Synthesized in Solution Plasma. *J. Phys. Chem. C* **2011**, *115*, 24569–24576. [CrossRef]
69. Sun, B.; Sato, M.; Clements, J.S. Optical study of active species produced by a pulsed streamer corona discharge in water. *J. Electrost.* **1997**, *39*, 189–202. [CrossRef]
70. Wang, R.; Che, G.S.; Wang, C.H.; Liu, C.Y.; Liu, B.S.; Ohtani, B.; Liu, Y.C.; Zhang, X.T. Alcohol Plasma Processed Surface Amorphization for Photocatalysis. *ACS Catal.* **2022**, *12*, 12206–12216. [CrossRef]
71. Sudare, T.; Ueno, T.; Watthanaphanit, A.; Saito, N. Accelerated nanoparticles synthesis in alcohol-water-mixture-based solution plasma. *Phys. Chem. Chem. Phys.* **2015**, *17*, 30255–30259. [CrossRef]
72. Wang, B.; Sun, B.; Zhu, X.M.; Yan, Z.Y.; Liu, Y.J.; Liu, H.; Liu, Q. Hydrogen production from alcohol solution by microwave discharge in liquid. *Int. J. Hydrogen Energy* **2016**, *41*, 7280–7291. [CrossRef]
73. Sun, B.; Wang, B.; Zhu, X.M.; Yan, Z.Y.; Liu, Y.J.; Liu, H. Study on the Emission Spectrum of Hydrogen Production with Microwave Discharge Plasma in Ethanol Solution. *Spectrosc. Spect. Anal.* **2016**, *36*, 823–826.
74. Xing, Y.M.; Wang, C.H.; Li, D.S.; Wang, R.; Liang, S.; Li, Y.Y.; Liu, Y.C.; Zhang, X.T. Solution Plasma Processing Single-Atom Au_1 on CeO_2 Nanosheet for Low Temperature Photo-Enhanced Mars-van Krevelen CO Oxidation. *Adv. Funct. Mater.* **2022**, *32*, 2207694. [CrossRef]
75. Sun, B. 5-Properties of Active Species of Discharge Plasma in Water. In *Discharge Plasma in Liquid and Its Applications*; Gu, Y.L., Bu, X., Eds.; Science Press: Beijing, China, 2013; p. 96.
76. Hayashi, Y.; Takada, N.; Wahyudiono; Kanda, H.; Goto, M. Hydrogen peroxide formation by electric discharge with fine bubbles. *Plasma Chem. Plasma Process.* **2017**, *37*, 125–135. [CrossRef]
77. Sun, B. 1-Low Temperature Plasma. In *Discharge Plasma in Liquid and Its Applications*; Gu, Y.L., Bu, X., Eds.; Science Press: Beijing, China, 2013; p. 8.
78. Pitchaimuthu, S.; Honda, K.; Suzuki, S.; Naito, A.; Suzuki, N.; Katsumata, K.; Nakata, K.; Ishida, N.; Kitamura, N.; Idemoto, Y.; et al. Solution Plasma Process-Derived Defect-Induced Heterophase Anatase/Brookite TiO_2 Nanocrystals for Enhanced Gaseous Photocatalytic Performance. *ACS Omega* **2018**, *3*, 898–905. [CrossRef] [PubMed]
79. Mizukoshi, Y.; Ohwada, M.; Seino, S.; Horibe, H.; Nishimura, Y.; Terashima, C. Synthesis of oxygen-deficient blue titanium oxide by discharge plasma generated in aqueous ammonia solution. *Appl. Surf. Sci.* **2019**, *489*, 255–261. [CrossRef]

80. Zhang, X.L.; Li, Z.; Zhan, Z.B.; Di, L.B. Preparation of F-Doped TiO_2 Photocatalysts by Gas–Liquid Plasma at Atmospheric Pressure. *Top. Catal.* **2017**, *60*, 980–986. [CrossRef]
81. Panomsuwan, G.; Watthanaphanit, A.; Ishizaki, T.; Saito, N. Water-plasma-assisted synthesis of black titania spheres with efficient visible-light photocatalytic activity. *Phys. Chem. Chem. Phys.* **2015**, *17*, 13794–13799. [CrossRef]
82. Jedsukontorn, T.; Ueno, T.; Saito, N.; Hunsom, M. Narrowing band gap energy of defective black TiO_2 fabricated by solution plasma process and its photocatalytic activity on glycerol transformation. *J. Alloys Compd.* **2018**, *757*, 188–199. [CrossRef]
83. Jedsukontorn, T.; Ueno, T.; Saito, N.; Hunsom, M. Facile preparation of defective black TiO_2 through the solution plasma process: Effect of parametric changes for plasma discharge on its structural and optical properties. *J. Alloys Compd.* **2017**, *726*, 567–577. [CrossRef]
84. Kim, K.; Chae, S.; Choi, P.G.; Itoh, T.; Saito, N.; Masuda, Y. Facile synthesis of ZnO nanobullets by solution plasma without chemical additives. *RSC Adv.* **2021**, *11*, 26785–26790. [CrossRef] [PubMed]
85. Saito, G.; Nakasugi, Y.; Yamashita, T.; Akiyama, T. Solution plasma synthesis of ZnO flowers and their photoluminescence properties. *Appl. Surf. Sci.* **2014**, *290*, 419–424. [CrossRef]
86. Yao, W.-T.; Yu, S.-H.; Zhou, Y.; Jiang, J.; Wu, Q.-S.; Zhang, L.; Jiang, J. Formation of uniform CuO nanorods by spontaneous aggregation: Selective synthesis of CuO, Cu_2O, and Cu nanoparticles by a solid-liquid phase arc discharge process. *J. Phys. Chem. B* **2005**, *109*, 14011–14016. [CrossRef]
87. Kim, H.; Watthanaphanit, A.; Saito, N. Simple Solution Plasma Synthesis of Hierarchical Nanoporous MnO_2 for Organic Dye Removal. *ACS Sustain. Chem. Eng.* **2017**, *5*, 5842–5851. [CrossRef]
88. Sirotkin, N.A.; Khlyustova, A.V.; Titov, V.A.; Krayev, A.S.; Nikitin, D.I.; Dmitrieva, O.A.; Agafonov, A.V. Synthesis and Photocatalytic Activity of WO_3 Nanoparticles Prepared by Underwater Impulse Discharge. *Plasma Chem. Plasma Process.* **2020**, *40*, 571–587. [CrossRef]
89. Tong, D.G.; Wu, P.; Su, P.K.; Wang, D.Q.; Tian, H.Y. Preparation of zinc oxide nanospheres by solution plasma process and their optical property, photocatalytic and antibacterial activities. *Mater. Lett.* **2012**, *70*, 94–97. [CrossRef]
90. Kang, J.; Li, O.L.; Saito, N. Synthesis of structure-controlled carbon nano spheres by solution plasma process. *Carbon* **2013**, *60*, 292–298. [CrossRef]
91. Romero Valenzuela, A.E.; Chokradjaroen, C.; Choeichom, P.; Wang, X.Y.; Kim, K.; Saito, N. Carbon Fibers Prepared via Solution Plasma-Generated Seeds. *Materials* **2023**, *16*, 906. [CrossRef]
92. Chokradjaroen, C.; Watanabe, H.; Ishii, T.; Ishizaki, T. Simultaneous synthesis of graphite-like and amorphous carbon materials via solution plasma and their evaluation as additive materials for cathode in Li-O_2 battery. *Sci. Rep.* **2021**, *11*, 6261. [CrossRef]
93. Tong, D.G.; Luo, Y.Y.; Chu, W.; Guo, Y.C.; Tian, W. Cutting of Carbon Nanotubes Via Solution Plasma Processing. *Plasma Chem. Plasma Process.* **2010**, *30*, 897–905. [CrossRef]
94. Ishizaki, T.; Chiba, S.; Kaneko, Y.; Panomsuwan, G. Electrocatalytic activity for the oxygen reduction reaction of oxygen-containing nanocarbon synthesized by solution plasma. *J. Mater. Chem. A* **2014**, *2*, 10589–10598. [CrossRef]
95. Treepet, S.; Chokradjaroen, C.; Kim, K.; Saito, N.; Watthanaphanit, A. Saccharide-originated fluorescent carbon dots synthesized by in-liquid plasma with controlled orderliness of carbon core through precursor alteration for selective and rapid metal ion detection. *Mater. Today Chem.* **2022**, *26*, 101139. [CrossRef]
96. Lee, S.H.; Heo, Y.K.; Bratescu, M.A.; Ueno, T.; Saito, N. Solution plasma synthesis of a boron-carbon-nitrogen catalyst with a controllable bond structure. *Phys. Chem. Chem. Phys.* **2017**, *19*, 15264–15272. [CrossRef] [PubMed]
97. Li, O.L.; Chiba, S.; Wada, Y.; Panomsuwan, G.; Ishizaki, T. Synthesis of graphitic-N and amino-N in nitrogen-doped carbon via a solution plasma process and exploration of their synergic effect for advanced oxygen reduction reaction. *J. Mater. Chem. A* **2017**, *5*, 2073–2082. [CrossRef]
98. Panomsuwan, G.; Saito, N.; Ishizaki, T. Simple one-step synthesis of fluorine-doped carbon nanoparticles as potential alternative metal-free electrocatalysts for oxygen reduction reaction. *J. Mater. Chem. A* **2015**, *3*, 9972–9981. [CrossRef]
99. Panomsuwan, G.; Saito, N.; Ishizaki, T. Nitrogen-doped carbon nanoparticles derived from acrylonitrile plasma for electrochemical oxygen reduction. *Phys. Chem. Chem. Phys.* **2015**, *17*, 6227–6232. [CrossRef]
100. Panomsuwan, G.; Saito, N.; Ishizaki, T. From cyano-aromatic molecules to nitrogen-doped carbons by solution plasma for the oxygen reduction reaction in alkaline medium. *Mater. Today Proc.* **2015**, *2*, 4302–4308. [CrossRef]
101. Niu, J.Q.; Chokradjaroen, C.; Saito, N. Graphitic N-doped graphene via solution plasma with a single dielectric barrier. *Carbon* **2022**, *199*, 347–356. [CrossRef]
102. Chae, S.; Panomsuwan, G.; Bratescu, M.A.; Teshima, K.; Saito, N. p-Type Doping of Graphene with Cationic Nitrogen. *ACS Appl. Nano Mater.* **2019**, *2*, 1350–1355. [CrossRef]
103. Kim, D.-Y.; Li, O.L.; Kang, J. Novel synthesis of highly phosphorus-doped carbon as an ultrahigh-rate anode for sodium ion batteries. *Carbon* **2020**, *168*, 448–457. [CrossRef]
104. Panomsuwan, G.; Saito, N.; Ishizaki, T. Nitrogen-Doped Carbon Nanoparticle-Carbon Nanofiber Composite as an Efficient Metal-Free Cathode Catalyst for Oxygen Reduction Reaction. *ACS Appl. Mater. Interfaces* **2016**, *8*, 6962–6971. [CrossRef] [PubMed]
105. Chokradjaroen, C.; Kato, S.; Fujiwara, K.; Watanabe, H.; Ishii, T.; Ishizaki, T. A comparative study of undoped, boron-doped, and boron/fluorine dual-doped carbon nanoparticles obtained via solution plasma as catalysts for the oxygen reduction reaction. *Sustain. Energy Fuels* **2020**, *4*, 4570–4580. [CrossRef]

106. Hyun, K.; Ueno, T.; Li, O.L.; Saito, N. Synthesis of heteroatom-carbon nanosheets by solution plasma processing using N-methyl-2-pyrrolidone as precursor. *RSC Adv.* **2016**, *6*, 6990–6996. [CrossRef]
107. Panomsuwan, G.; Chiba, S.; Kaneko, Y.; Saito, N.; Ishizaki, T. In situ solution plasma synthesis of nitrogen-doped carbon nanoparticles as metal-free electrocatalysts for the oxygen reduction reaction. *J. Mater. Chem. A* **2014**, *2*, 18677–18686. [CrossRef]
108. Panomsuwan, G.; Saito, N.; Ishizaki, T. Electrocatalytic oxygen reduction activity of boron-doped carbon nanoparticles synthesized via solution plasma process. *Electrochem. Commun.* **2015**, *59*, 81–85. [CrossRef]
109. Panomsuwan, G.; Saito, N.; Ishizaki, T. Electrocatalytic oxygen reduction on nitrogen-doped carbon nanoparticles derived from cyano-aromatic molecules via a solution plasma approach. *Carbon* **2016**, *98*, 411–420. [CrossRef]
110. Kim, D.W.; Li, O.L.; Saito, N. Enhancement of ORR catalytic activity by multiple heteroatom-doped carbon materials. *Phys. Chem. Chem. Phys.* **2015**, *17*, 407–413. [CrossRef]
111. Hieda, J.; Saito, N.; Takai, O. Exotic shapes of gold nanoparticles synthesized using plasma in aqueous solution. *J. Vac. Sci. Technol. A* **2008**, *26*, 854–856. [CrossRef]
112. Sudare, T.; Ueno, T.; Watthanaphanit, A.; Saito, N. Verification of Radicals Formation in Ethanol-Water Mixture Based Solution Plasma and Their Relation to the Rate of Reaction. *J. Phys. Chem. A* **2015**, *119*, 11668–11673. [CrossRef]
113. Hu, X.L.; Cho, S.-P.; Takai, O.; Saito, N. Rapid Synthesis and Structural Characterization of Well-Defined Gold Clusters by Solution Plasma Sputtering. *Cryst. Growth Des.* **2012**, *12*, 119–123. [CrossRef]
114. Zhang, J.B.; Hu, X.L.; Yang, B.Q.; Su, N.; Huang, H.H.; Cheng, J.X.; Yang, H.; Saito, N. Novel synthesis of PtPd nanoparticles with good electrocatalytic activity and durability. *J. Alloys Compd.* **2017**, *709*, 588–595. [CrossRef]
115. Thai, V.-P.; Nguyen, H.D.; Saito, N.; Takahashi, K.; Sasaki, T.; Kikuchi, T. Precise size-control and functionalization of gold nanoparticles synthesized by plasma-liquid interactions: Using carboxylic, amino, and thiol ligands. *Nanoscale Adv.* **2022**, *4*, 4490–4501. [CrossRef] [PubMed]
116. Titov, V.; Nikitin, D.; Naumova, I.; Losev, N.; Lipatova, I.; Kosterin, D.; Pleskunov, P.; Perekrestov, R.; Sirotkin, N.; Khlyustova, A.; et al. Dual-Mode Solution Plasma Processing for the Production of Chitosan/Ag Composites with the Antibacterial Effect. *Materials* **2020**, *13*, 4821. [CrossRef] [PubMed]
117. Nam, S.; Mubarakali, D.; Kim, J. Characterization of Alginate/Silver Nanobiocomposites Synthesized by Solution Plasma Process and Their Antimicrobial Properties. *J. Nanomater.* **2016**, *2016*, 4712813. [CrossRef]
118. Shi, J.J.; Hu, X.L.; Zhang, J.B.; Tang, W.P.; Li, H.T.; Shen, X.D.; Saito, N. One-step facile synthesis of Pd nanoclusters supported on carbon and their electrochemical property. *Prog. Nat. Sci. Mater. Int.* **2014**, *24*, 593–598. [CrossRef]
119. Watthanaphanit, A.; Panomsuwan, G.; Saito, N. A novel one-step synthesis of gold nanoparticles in an alginate gel matrix by solution plasma sputtering. *RSC Adv.* **2014**, *4*, 1622–1629. [CrossRef]
120. Mukasa, S.; Masuda, T.; Kimura, E.; Sumoto, Y.; Toyota, H.; Nomura, S. Synthesis of Tin Nanoparticles by Pulse Discharge in Water and Aqueous Gelatin Solution. *J. Jpn. Inst. Energy* **2018**, *97*, 186–190. [CrossRef]
121. Hu, X.L.; Shen, X.D.; Takai, O.; Saito, N. Facile fabrication of PtAu alloy clusters using solution plasma sputtering and their electrocatalytic activity. *J. Alloys Compd.* **2013**, *552*, 351–355. [CrossRef]
122. Hu, X.L.; Shi, J.J.; Zhang, J.B.; Tang, W.P.; Zhu, H.K.; Shen, X.D.; Saito, N. One-step facile synthesis of carbon-supported PdAu nanoparticles and their electrochemical property and stability. *J. Alloys Compd.* **2015**, *619*, 452–457. [CrossRef]
123. Trad, M.; Nomine, A.; Noel, C.; Ghanbaja, J.; Tabbal, M.; Belmonte, T. Evidence of alloy formation in CoNi nanoparticles synthesized by nanosecond-pulsed discharges in liquid nitrogen. *Plasma Process. Polym.* **2020**, *17*, e1900255. [CrossRef]
124. Panomsuwan, G.; Wongcharoen, S.; Chokradcharoen, C.; Tipplook, M.; Jongprateep, O.; Saito, N. Au nanoparticle-decorated TiO_2 hollow fibers with enhanced visible-light photocatalytic activity toward dye degradation. *RSC Adv.* **2022**, *12*, 193–200. [CrossRef] [PubMed]
125. Hu, X.L.; Ge, C.; Su, N.; Huang, H.H.; Xu, Y.Q.; Zhang, J.B.; Shi, J.J.; Shen, X.D.; Saito, N. Solution plasma synthesis of Pt/ZnO/KB for photo-assisted electro-oxidation of methanol. *J. Alloys Compd.* **2017**, *692*, 848–854. [CrossRef]
126. Kim, S.-M.; Jo, Y.-G.; Lee, M.-H.; Saito, N.; Kim, J.-W.; Lee, S.-Y. The plasma-assisted formation of Ag@Co_3O_4 core-shell hybrid nanocrystals for oxygen reduction reaction. *Electrochim. Acta* **2017**, *233*, 123–133. [CrossRef]
127. Nakasugi, Y.; Saito, G.; Yamashita, T.; Sakaguchi, N.; Akiyama, T. Solution plasma synthesis of Au nanoparticles for coating titanium dioxide to enhance its photocatalytic activity. *Thin Solid Films* **2015**, *583*, 135–141. [CrossRef]
128. Park, J.; Lam, S.S.; Park, Y.-K.; Kim, B.-J.; An, K.-H.; Jung, S.-C. Fabrication of Ni/TiO_2 visible light responsive photocatalyst for decomposition of oxytetracycline. *Environ. Res.* **2023**, *216*, 114657. [CrossRef]
129. Panomsuwan, G.; Zettsu, N.; Saito, N. Gold Nanoparticles Supported on $SrTiO_3$ by Solution Plasma Sputter Deposition for Enhancing UV- and Visible-light Photocatalytic Efficiency. *Mater. Res. Soc. Symp. Proc.* **2013**, *1509*, 914. [CrossRef]
130. Zhang, Y.P.; Ding, P.; Wu, W.B.; Kimura, H.; Shen, Y.H.; Wu, D.; Xie, X.B.; Hou, C.X.; Sun, X.Q.; Yang, X.Y.; et al. Facile synthesis of reduced graphene oxide@Co_3O_4 composites derived from assisted liquid-phase plasma electrolysis for high-performance hybrid supercapacitors. *Appl. Surf. Sci.* **2023**, *609*, 155188. [CrossRef]
131. Zhong, Z.Y.; Wang, C.C.; Han, R.Y.; Gao, M.; Huang, Y.F.; Ramakrishna, S. Synthesis of zinc oxide/carbon fiber composites with improved piezoelectric response by plasma-liquid interaction. *Compos. Commun.* **2023**, *38*, 101495. [CrossRef]
132. Lee, C.W.; Lee, S.-G.; Noh, J.H.; Jung, H.S.; Chung, K.-J.; Hong, K.S.; Kim, D.W.; Hwang, Y.S.; Kim, D.-W. Synthesis of carbon-incorporated titanium oxide nanocrystals by pulsed solution plasma: Electrical, optical investigation and nanocrystals analysis. *RSC Adv.* **2015**, *5*, 9497–9502. [CrossRef]

133. Phan, P.Q.; Chae, S.; Pornaroontham, P.; Muta, Y.; Kim, K.; Wang, X.Y.; Saito, N. In situ synthesis of copper nanoparticles encapsulated by nitrogen-doped graphene at room temperature via solution plasma. *RSC Adv.* **2020**, *10*, 36627–36635. [CrossRef]
134. Phan, P.Q.; Naraprawatphong, R.; Pornaroontham, P.; Park, J.; Chokradjaroen, C.; Saito, N. N-Doped few-layer graphene encapsulated Pt-based bimetallic nanoparticles via solution plasma as an efficient oxygen catalyst for the oxygen reduction reaction. *Mater. Adv.* **2021**, *2*, 322–335. [CrossRef]
135. Dack, M.R.J. The importance of solvent internal pressure and cohesion to solution phenomena. *Chem. Soc. Rev.* **1975**, *4*, 211–229. [CrossRef]
136. Schneider, J.; Matsuoka, M.; Takeuchi, M.; Zhang, J.L.; Horiuchi, Y.; Anpo, M.; Bahnemann, D.W. Understanding TiO_2 Photocatalysis: Mechanisms and Materials. *Chem. Rev.* **2014**, *114*, 9919–9986. [CrossRef]
137. Yu, J.G.; Li, X.; Jin, Z.L.; Tang, H.; Liu, E.Z. Preface to Solar Photocatalysis. *Chin. J. Struct. Chem.* **2022**, *41*, 2206001–2206002.
138. Tao, S.R.; Wan, S.J.; Huang, Q.Y.; Li, C.M.; Yu, J.G.; Cao, S.W. Molecular Engineering of g-C_3N_4 with Dibenzothiophene Groups as Electron Donor for Enhanced Photocatalytic H_2-Production. *Chin. J. Struct. Chem.* **2022**, *41*, 2206048–2206054.
139. Zhang, B.; Hu, X.Y.; Liu, E.Z.; Fan, J. Novel S-scheme 2D/2D BiOBr/g-C_3N_4 heterojunctions with enhanced photocatalytic activity. *Chin. J. Catal.* **2021**, *42*, 1519–1529. [CrossRef]
140. Yu, F.; Wang, C.H.; Li, Y.Y.; Ma, H.; Wang, R.; Liu, Y.C.; Suzuki, N.; Terashima, C.; Ohtani, B.; Ochiai, T.; et al. Enhanced Solar Photothermal Catalysis over Solution Plasma Activated TiO_2. *Adv. Sci.* **2020**, *7*, 2000204. [CrossRef]
141. Cronemeyer, D.C. Infrared Absorption of Reduced Rutile TiO_2 Single Crystals. *Phys. Rev.* **1959**, *113*, 1222–1226. [CrossRef]
142. Asahi, R.; Morikawa, T.; Ohwaki, T.; Aoki, K.; Taga, Y. Visible-light photocatalysis in nitrogen-doped titanium oxides. *Science* **2001**, *293*, 269–271. [CrossRef]
143. Che, G.S.; Wang, D.D.; Wang, C.H.; Yu, F.; Li, D.S.; Suzuki, N.; Terashima, C.; Fujishima, A.; Liu, Y.C.; Zhang, X.T. Solution plasma boosts facet-dependent photoactivity of decahedral $BiVO_4$. *Chem. Eng. J.* **2020**, *397*, 125381. [CrossRef]
144. Chen, X.B.; Liu, L.; Yu, P.Y.; Mao, S.S. Increasing Solar Absorption for Photocatalysis with Black Hydrogenated Titanium Dioxide Nanocrystals. *Science* **2011**, *331*, 746–750. [CrossRef] [PubMed]
145. Yang, J.K.; Zhang, X.T.; Liu, H.; Wang, C.H.; Liu, S.P.; Sun, P.P.; Wang, L.L.; Liu, Y.C. Heterostructured TiO_2/WO_3 porous microspheres: Preparation, characterization and photocatalytic properties. *Catal. Today* **2013**, *201*, 195–202. [CrossRef]
146. Shen, Y.; Nitta, A.; Takashima, M.; Ohtani, B. Do Particles Interact Electronically?—Proof of Interparticle Charge-transfer Excitation between Adjoined Anatase and Rutile Particles. *Chem. Lett.* **2021**, *50*, 80–83. [CrossRef]
147. Chen, G.Y.; Takashima, M.; Ohtani, B. Direct Amorphous-structure Analysis: How are Surface/Bulk Structure and Activity of Titania Photocatalyst Particles Changed by Milling? *Chem. Lett.* **2021**, *50*, 644–648. [CrossRef]
148. Łuczak, J.; Pancielejko, A.; Chen, G.Y.; Takashima, M.; Zaleska-Medynska, A.; Ohtani, B. How Do Ionic Liquids Affect the Surface Structure of Titania Photocatalyst? An Electron-Trap Distribution-Analysis Study. *J. Phys. Chem. C* **2021**, *125*, 28143–28149. [CrossRef]
149. Shan, J.Q.; Ye, C.; Jiang, Y.L.; Jaroniec, M.; Zheng, Y.; Qiao, S.Z. Metal-metal interactions in correlated single-atom catalysts. *Sci. Adv.* **2022**, *8*, eabo0762. [CrossRef] [PubMed]
150. Chen, Y.X.; Wang, L.J.; Yao, Z.B.; Hao, L.D.; Tan, X.Y.; Masa, J.T.; Robertson, A.L.; Sun, Z.Y. Tuning the Coordination Structure of Single Atoms and Their Interaction with the Support for Carbon Dioxide Electroreduction. *Acta Phys.-Chim. Sin.* **2022**, *38*, 2207024. [CrossRef]
151. Liu, L.C.; Corma, A. Metal Catalysts for Heterogeneous Catalysis: From Single Atoms to Nanoclusters and Nanoparticles. *Chem. Rev.* **2018**, *118*, 4981–5079. [CrossRef]
152. Wang, C.P.; Wang, Z.; Mao, S.J.; Chen, Z.R.; Wang, Y. Coordination environment of active sites and their effect on catalytic performance of heterogeneous catalysts. *Chin. J. Catal.* **2022**, *43*, 928–955. [CrossRef]
153. Xing, Y.M. Liquid Phase Plasma Preparation of Single-Atom Metal on CeO_2 Nanosheet for Photo-Enhanced Catalytic Oxidation Performance. Ph.D. Thesis, The Northeast Normal University, Changchun, China, 2023.
154. Huang, Y.; Wang, C.H.; Wang, R.; Zhang, Y.Y.; Li, D.S.; Zhu, H.C.; Wang, G.R.; Zhang, X.T. Ethanol Solution Plasma Loads Carbon Dots onto 2D HNb_3O_8 for Enhanced Photocatalysis. *ACS Appl. Mater. Interfaces* **2023**, *15*, 1157–1166. [CrossRef]
155. Li, Y.N.; Wang, Y.L.; Lin, J.F.; Shi, Y.M.; Zhu, K.Y.; Xing, Y.M.; Li, X.F.; Jia, Y.W.; Zhang, X.T. Solution-plasma-induced oxygen vacancy enhances MoO_x/Pt electrocatalytic counter electrode for bifacial dye-sensitized solar cells. *Front. Energy Res.* **2022**, *10*, 924515. [CrossRef]
156. Li, D.S.; Lu, J.X.; Wang, C.H.; Xing, Y.M.; Liang, S.; Wang, R.; Zhang, X.T.; Liu, Y.C. Photo-plasma catalytic degradation of high concentration volatile organic compounds. *Appl. Catal. A* **2022**, *647*, 118908. [CrossRef]
157. Carreon, M.L. Plasma catalysis: A brief tutorial. *Plasma Res. Express* **2019**, *1*, 043001. [CrossRef]
158. Neyts, E.C.; Ostrikov, K.K.; Sunkara, M.K.; Bogaerts, A. Plasma Catalysis: Synergistic Effects at the Nanoscale. *Chem. Rev.* **2015**, *115*, 13408–13446. [CrossRef] [PubMed]

Disclaimer/Publisher's Note: The statements, opinions and data contained in all publications are solely those of the individual author(s) and contributor(s) and not of MDPI and/or the editor(s). MDPI and/or the editor(s) disclaim responsibility for any injury to people or property resulting from any ideas, methods, instructions or products referred to in the content.